AN ABSTRACT OF THE THESIS OF

Etienne M. Mullin for the degree of Master of Science in Nuclear Engineering presented on May 6, 2015.

Title: High Pressure Condensation in an SMR Containment

Abstract approved: ____

Qiao Wu

The Oregon State University Multi-Application Small Light Water Reactor test facility is employed in a series tests to evaluate condensation heat transfer in small, high pressure containment vessels characteristic of small modular reactor designs under development. This integral system test facility was constructed to demonstrate the feasibility of a pioneering SMR design and features a scaled containment vessel and cooling pool heat sink. The tests performed involve supplying steam into the containment and observing the condensation rates occurring on the heat transfer surface. The test data is reduced to quantify condensation heat transfer rates and heat transfer coefficients. Particular attention is paid to the influence of system pressure and noncondensable gas inventory.

High Pressure Condensation in an SMR Containment

by

Etienne M. Mullin

A THESIS

Submitted to

Oregon State University

in partial fulfillment of

the requirements for the

degree of

Master of Science in Nuclear Engineering

Presented May 6, 2015

Commencement June, 2016

Master of Science thesis of Etienne M. Mullin presented on May 6, 2015.

APPROVED:

Major Professor, representing Nuclear Engineering

Head of the Department of Nuclear Engineering and Radiation Health Physics

Dean of the Graduate School

I understand that my thesis will become part of the permanent collect of Oregon State University libraries. My signature below authorizes the release of my thesis to any reader upon request.

Etienne M. Mullin, Author

ACKNOWLEDGEMENTS

First and foremost, I thank my advisor, Dr. Qiao Wu, for providing me the opportunity to be involved in this project and for supporting me during my education and research. I thank the entire faculty of NERHP department for imparting their knowledge and experience unto me over the last 7 years. The department has done an exemplary job at preparing its students to be successful in this field.

I would like to thank the U.S. Department of Energy for funding this research as part of the Nuclear Energy University Programs. Their contributions are critical to ensuring advancements in the field and supporting the education of young members in our field.

I would like to thank the current and past members of the MASLWR/NIST-1 team for all they have done in developing and operating a successful testing program and making this experimental research possible. The incredible effort they put towards the goals of the program is well recognized. The team were very helpful in answering questions and supporting my work.

I would like to thank the testing organization at NuScale Power LLC. for permitting use of the test facility data in academic investigations. Discussions I have had with the engineers at NuScale, notably with Claudio Delfino and Jose Reyes, have been influential in developing my analytical methods and drawing conclusions from the data. I would also like to thank my supervisor, Bill Galyean, and numerous colleagues with whom I work with in the Probabilistic Risk Assessment Group at NuScale. They have long supported me in balancing my education and the work I am involved with there. This at times has been challenging.

I would like to thank my family and friends for supporting me throughout my education. Finally, I would also like to thank all of the students I have worked with over the years. Sharing these experiences has made the hard work much more manageable.

TABLE OF CONTENTS

Page

TABLE OF CONTENTS (CONTINUED)

Page

LIST OF FIGURES

LIST OF FIGURES (CONTINUED)

Figure Page

LIST OF TABLES

NOMENCLATURE

SMR	Small Modular Reactor
OSU	Oregon State University
MASLWR	Multi-Application Small Light Water Reactor
ECCS	Emergency Core Cooling System
LOCA	Loss of Coolant Accident
PCCS	Passive Containment Cooling System
BWR	Boiling Water Reactor
PWR	Pressurized Water Reactor
HPC	High Pressure Containment
HTP	Heat Transfer Plate
CPV	Cooling Pool Vessel
RPV	Reactor Pressure Vessel
ADS	Automatic Depressurization System
P&ID	Piping and Instrumentation Diagram

SYMBOLS

$\dot{Q}"$	heat flux
T	temperature
R	thermal resistance
h	heat transfer coefficient
x	distance
k	thermal conductivity
δ	film thickness
Nu	Nusselt number
ρ	density
g	acceleration of gravity
h_{lv}	heat of vaporization
μ	dynamic viscosity
ω	noncondensable weight/mass fraction
L	length
P	pressure
A	area
V	volume
m	mass
E	energy
u	specific internal energy
$\bar{R}$	universal gas constant
MW	molecular weight
Cp	specific heat capacity at constant pressure
H	enthalpy
h	specific enthalpy

SUBSCRIPTS

sat	saturation
w	wall/surface
x	local
l	liquid (general)
v	vapor (general)
∞	infinity (at bulk)
L	length (average)
liq	liquid (referring to condensate pool)
vap	vapor (referring to vapor space)
NCG	noncondensable gas
$sens$	sensible heat
$8iX$	HTP thermocouple (elevation i, 'depth' X)

1 Introduction

Steam condensation on cool surfaces is a highly effective heat transfer mechanism employed in nuclear system design to provide passive cooling during design basis events and severe accidents. As an emphasis on long-term passive coolability has grown in recent decades, nuclear technology organizations are increasingly relying on condensation based safety systems to bolster the safety case of emerging reactor designs. While containment condensation has long been credited in existing plants to limit containment pressurization during severe accidents, newer designs have focused on enhancing the phenomenon to reliably provide long term passive cooling to address design basis events. The NuScale Power Module™, an innovative Small Modular Reactor (SMR) design, was conceptualized with this goal in mind as containment condensation drives its unique Emergency Core Cooling System. Characterization of condensation rates in this unique containment configuration under anticipated accident conditions is critical to ensuring adequate heat removal and maintaining coolability of the reactor core. The experimental research presented in this thesis explores condensation rates in a scaled SMR containment with an emphasis on the effect of steam pressures and the presence of non-condensable gasses.

The Multi-Application Small Light Water Reactor (MASLWR) concept, the precursor to the NuScale Power Module™, was developed in the early 2000's through a partnership between Idaho National Labs, Nexant-Bechtel, and Oregon State University with support from the Department of Energy (DOE) under the auspices of the Nuclear Energy Research Initiative. The MASLWR concept is a small pressurized water reactor that relies on natural circulation to provide core flow. The pressurizer and steam generator are integrated into the primary reactor vessel which lies within a high-pressure containment which in turn is submerged in a large cooling pool (Figure 1-1).

The MASLWR concept achieves passive safety through its Emergency Core Cooling System (ECCS). The ECCS consists of a set of valves near the top and bottom of the Reactor Pressure Vessel (RPV) that fail to the open position in the case of a loss of power or safety signal. Primary coolant from the RPV then flashes to steam in the containment as pressure equalizes between the vessels. Condensation, convection, and conduction move heat through the containment to the cooling pool to provide reliable long term cooling without the need for electrical power or operator action. While the NuScale Power Module™ design has evolved since the original MASLWR concept, the intent and design of the ECCS remains much the same.

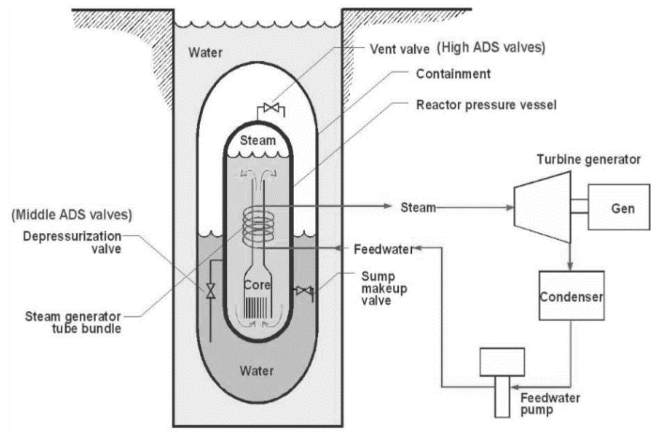

Figure 1-1: MASLWR concept

Aside from evaluating the design, safety, and economic attributes of the prototypic design, a major task of the DOE research initiative was to test the technical feasibility with an integrally scaled test facility. The facility, built on the Oregon State University (OSU) campus, is scaled to 1:3 height and features an electrically heated core with an integrated pressurizer and steam generator. The MASLWR test facility was used to research the stability of natural circulation driven primary flow as well as the performance of the ECCS. The DOE contract was concluded in 2003 with the completion of the sponsored test matrix and submission of an extensive final report [1]. In 2007, NuScale Power LLC. was formed to commercially pursue the technology and was granted exclusive rights to the design and OSU test facility through a technology transfer agreement with the university. Since then, an NQA-1 compliant testing program has been established about the facility for the purpose of developing and validating thermal hydraulic codes employed in the safety analysis of the prototypic plant.

An area of significant interest in the safety analysis of the MASLWR and NuScale design and the topic of this thesis is the performance of containment condensation. The pressures expected in the containment of the NuScale Power Module™ during a depressurization event are on the order of ten times greater than traditional reactor designs. The small size of the containment vessel with respect to the volume of primary coolant causes the equilibrium pressures to be much greater, while the increased curvature of the smaller vessel allows it to handle these pressures without excessively thick walls. Additionally, the small size of the containment and simplicity of the containment internals make it feasible to evacuate this space during normal operation, thus the concentration of noncondensable gas is far lower than traditional designs. This eliminates the need for additional insulation and improves condensate rates in the event of a depressurization into containment.

As shown in the literature, various studies have been conducted to experimentally characterize condensation rates for typical reactor containments. However, these experiments were generally performed at modest steam pressures with relatively large non-condensable gas concentrations. The pressure and gas concentrations expected during a blowdown event within the containment of the NuScale Power Module™ lie far outside the range of applicability of the widely employed containment condensation models available today. To bridge this gap in knowledge, a series of condensation tests have been performed within the containment of the MASLWR test facility. The goal of these tests was to introduce steam into the containment and explore the effect of pressure and initial air inventory on condensation rates.

A total of 13 tests were conducted during this investigation. The first set of 6 tests were conducted by supplying a constant rate of steam at two different flow rates with three different initial air inventories. These tests saw pressure continuously rise in the containment until termination of each test. The second set of 7 tests were performed with the goal of each reaching and maintaining a unique steam pressure. The collection of these quasi-steady tests characterizes condensation rates over the full range of achievable pressures while mitigating the influence of transient phenomena. This thesis presents and discusses the findings of these experiments.

This investigation contains inherent limitations which are disclosed throughout the report. These limitations are in large part due to utilization of the facility beyond its original intent. As part of the design certification process with the Nuclear Regulatory Commission, NuScale Power LLC. is required to prove that they have appropriately evaluated condensation rates in the geometry and unique conditions of the NuScale Power Module™ containment. The content of this thesis should not be considered an attempt to perform that task.

2 Background

2.1 Condensation Heat Transfer

Condensation describes the phase change of a fluid from vapor to liquid. This may occur when heat is removed from a vapor such that it is cooled to below its saturation temperature. Due to van der walls forces (surface tension), the super-saturated vapor must yet overcome a free energy penalty to form a liquid droplet. In a pure, unperturbed medium, this energy barrier generally prohibits phase change until subcooling of the vapor becomes very large (homogenous condensation). However, the presence of foreign particulates or microscopic surface textures drastically lessens this energy penalty and provides nucleation sites to seed the phase change (heterogeneous condensation).

Once a liquid-vapor interface is established, a reduction in pressure across the boundary drives vapor to the subcooled liquid surface where it may condense. Accompanying the phase change is the release of latent heat. This heat must be continuously removed from the liquid phase to maintain subcooling and the driving pressure gradient. This exchange of latent heat occurs over a small change in temperature across the phase boundary, implying a highly effective heat transfer mechanism. [2]

Practical application of condensation in heat transfer systems is limited primarily to surface condensation where the surface provides droplet nucleation sites or anchors a liquid film. The surface must also allow for continuous removal of the latent heat to drive condensation. While not discussed further in this thesis, volume condensation also has important applications such as pressure mediation in two-phase systems from the use sprays and spargers.

Surface condensation can occur in either the filmwise or dropwise modes. Filmwise condensation occurs when condensate completely wets the cooled surface and produces a film that grows continuously along the direction of flow. Dropwise condensation can occur on hydrophobic surfaces where the condensate forms beads that fall under gravity and wipe clean the surface below. Although dropwise condensation has been shown to more effectively remove heat than filmwise condensation (because a thick condensate film adds conductive resistance), the special surface finishes and treatments required to maintain dropwise condensation are largely impractical in heat transfer systems. [3]

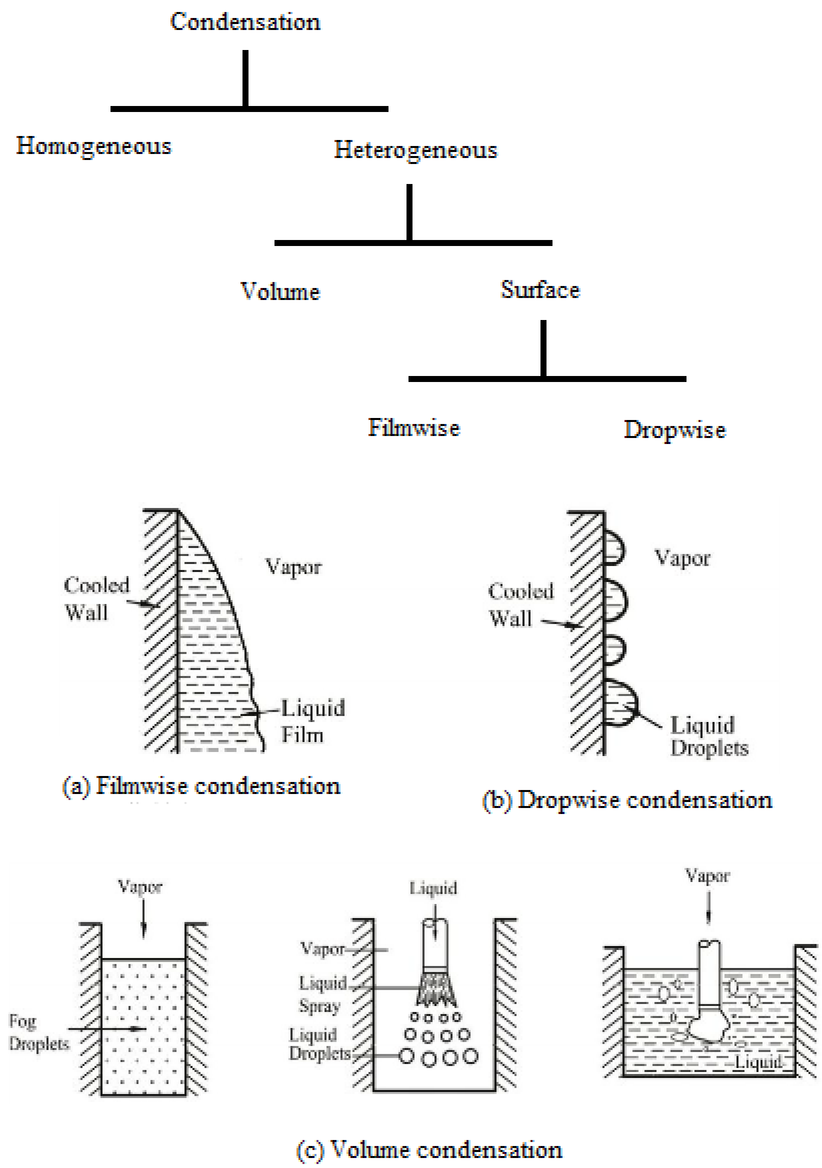

Figure 2-1: Types of condensation [4]

The phenomenon of condensation is observed when the rate of arrival of vapor molecules toward a liquid interface is greater than the departure rate. These rates can be approximated employing the kinetic theory of gasses for appropriate temperatures and pressures across a phase boundary. However, the theoretical condensation rates calculated with this method are generally higher than experimental observations at least in part because the theory fails to consider the complex molecular interactions involved. [2]

As a heat transfer problem, the condensation process can be described as a series of thermal resistances. Diffusion and convection dictate the supply of steam to the interface. A phase change occurs at the surface and then conduction removes the heat from the film. The heat transfer rate is driven by a temperature difference across each of these resistance.

These resistances are often quantified with their reciprocal, heat transfer coefficients. As such, a separate heat transfer coefficient could be defined for each resistance to heat transfer. Alternatively, an overall heat transfer coefficient can be defined for the combination of resistances. Generally, the two main components to the overall heat transfer coefficient are from phase change (condensation heat transfer coefficient) and conduction through the film (film heat transfer coefficient).

$$\dot{Q}" = \frac{(T_{vapor} - T_{film})}{R_{condensation}} = \frac{(T_{film} - T_{wall})}{R_{film}} = h_{total} \cdot (T_{vapor} - T_{wall}) \tag{2.1}$$

$$h_{total} = \left(\frac{1}{h_{condensation}} + \frac{1}{h_{film}}\right)^{-1} \tag{2.2}$$

Evaluating the condensation heat transfer coefficient can be problematic. The complex molecular interactions involved in the phase change at the interface are difficult to characterize, and analytical models for the rates of phase change are based on empirical observations of interaction rates. The conductive resistance in the film, however, is well characterized with analytical methods.

Condensation proves to be a potent heat transfer mechanism because the thermal resistance to the phase change is generally very low (i.e. the condensation heat transfer coefficient is very high). When a pure vapor is at saturation, the phase change to liquid occurs over a very small, often immeasurable, change in temperature. What generally limits the process is the rate at which conduction through the condensate can remove the latent heat being released so that the film remains subcooled. In general, the condensate film is thin and heat transfer rates are high. When condensation occurs in the dropwise form, heat transfer rates are even higher. [4]

2.1.1 Nusselt

Wilhelm Nusselt [5] was the one of first to reduce the complexity of the condensation process to produce an analytical solution for heat transfer, which remains, almost 100 years later, the defining work in the field. Nusselt examined filmwise condensation of a stagnant vapor occurring on a cooled vertical wall. In his model, a condensate film flows down the surface of a plate and grows in thickness as mass transport occurs across the phase boundary.

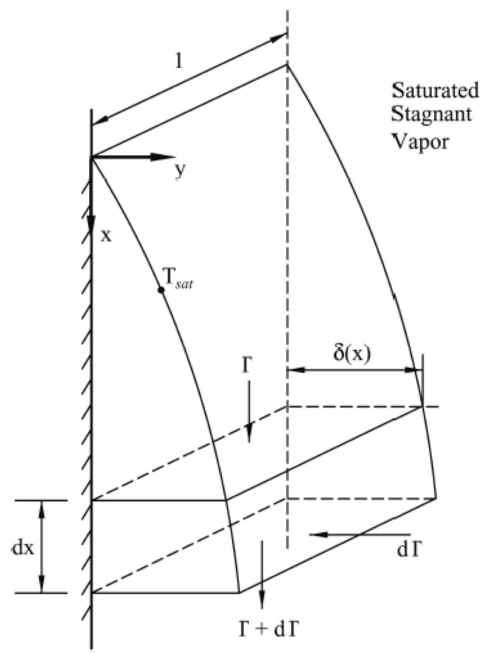

Figure 2-2: Nusselt's control volume [4]

Nusselt's elegant analytical solution relies on several simplifying assumptions:

1. Laminar film flow
    a. No advection across film
    b. Heat transfer through film by conduction only
2. Pure, saturated, stagnant vapor
3. Negligible shear stress at liquid vapor interface
4. Negligible subcooling of the condensate (no temperature jump at interface)
5. Isothermal wall
6. Constant fluid properties

The most important implication of Nusselt's simplifications is that the only resistance to heat transfer occurs through the film. That is, the overall heat transfer coefficient can be determined with a simple conduction calculation.

$$\dot{Q}''(x) = \frac{k}{\delta(x)}(T_{sat} - T_w) = h_{total}(x) \cdot (T_{sat} - T_w) \tag{2.3}$$

$$h_{total}(x) = \frac{k}{\delta(x)} \tag{2.4}$$

The problem is thus reduced to solving for the condensate film thickness as a function of position on the plate. This is done through integration of the momentum along the direction of film flow and application of the appropriate boundary conditions. Ultimately, Nusselt's model characterizes the condensate flow rate, film thickness, and heat transfer rate coefficient as a function of distance along the plate. His solution can be presented in various forms, including in terms of the dimensionless local Nusselt number:

$$Nu_x = \frac{h_x x}{k_l} = \left[\frac{\rho_l(\rho_l - \rho_v) g h_{lv} x^3}{4 k_l \mu_l \Delta T}\right]^{1/4} \tag{2.5}$$

2.1.2 Building on Nusselt's Work

In spite of the many simplifications made to develop his formulation, Nusselt's theory has been shown to predict condensation heat transfer coefficients quite well. The analytical solution is generally considered a conservative prediction of condensation rates as subsequent investigations have thoroughly evaluated Nusselt's simplifying assumptions and recognized additional phenomena that enhance condensation.

Stender [6] studied the effect of superheated vapor and Bromley [7] investigated the effects of subcooling of the condensate film. Sparrow and Gregg [8] considered inertial and convective terms within the film. Poots and Miles [9] evaluated the effect of variable fluid properties while Chen [10] included the influence of interfacial shear on the film surface.

Brauer [11] described the onset of waves and ripples at the liquid-vapor boundary at relatively low film Reynolds numbers ($Re_\delta \approx 30$) and observed an increase in condensation rates of up to 50% in some cases due to the increased interfacial area and decreased mean film thickness. The onset of turbulence in the film ($Re_\delta \approx 1800$) further increases condensation rates by introducing significant convective elements within the film boundary and increasing the interfacial area. Butterworth [12] proposed an empirical correlation for film condensation that covers laminar, wavy, and turbulent film flows. [13]

In the case of steam condensation, Nusselt's simplifications have shown to be widely acceptable for laminar flows and empirical adjustments extend Nusselt's basic theory to account for wavy and turbulent films. However, Sukhatme and Rohsenow [14] indicate that Nusselt's model breaks down when highly conductive fluids are considered such as for condensing metallic vapors. As the resistance to conduction is greatly reduced within the film, the heat transfer resistance at the phase change boundary becomes more important (the Nusselt formulation neglects this resistance).

2.2 Condensation in the Presence of Noncondensable Gas

While Nusselt's work remains the foundation for condensation studies, his model only considers the condensation of pure vapors. In many real world applications, non-condensable gases are present along with condensable vapor. Commonly of concern is the condensation of water vapor in the presence of air.

The process of condensation becomes significantly more complex in the presence of non-condensable gas which ultimately leads to dramatic reductions in condensation and heat transfer rates. The reduction in condensation rate can mostly be attributed to the buildup of noncondensable gases near the phase boundary. Condensation draws the vapor-gas mixture to the liquid interface but only the vapor crosses the boundary leaving noncondensable gases behind in high concentrations. The transport of vapor to the liquid film is then limited by the rate of diffusion of noncondensable gases away from the interface. In the presence of noncondensable gas, a second boundary layer is introduced to condensation analysis: the gas/vapor diffusion layer. [15]

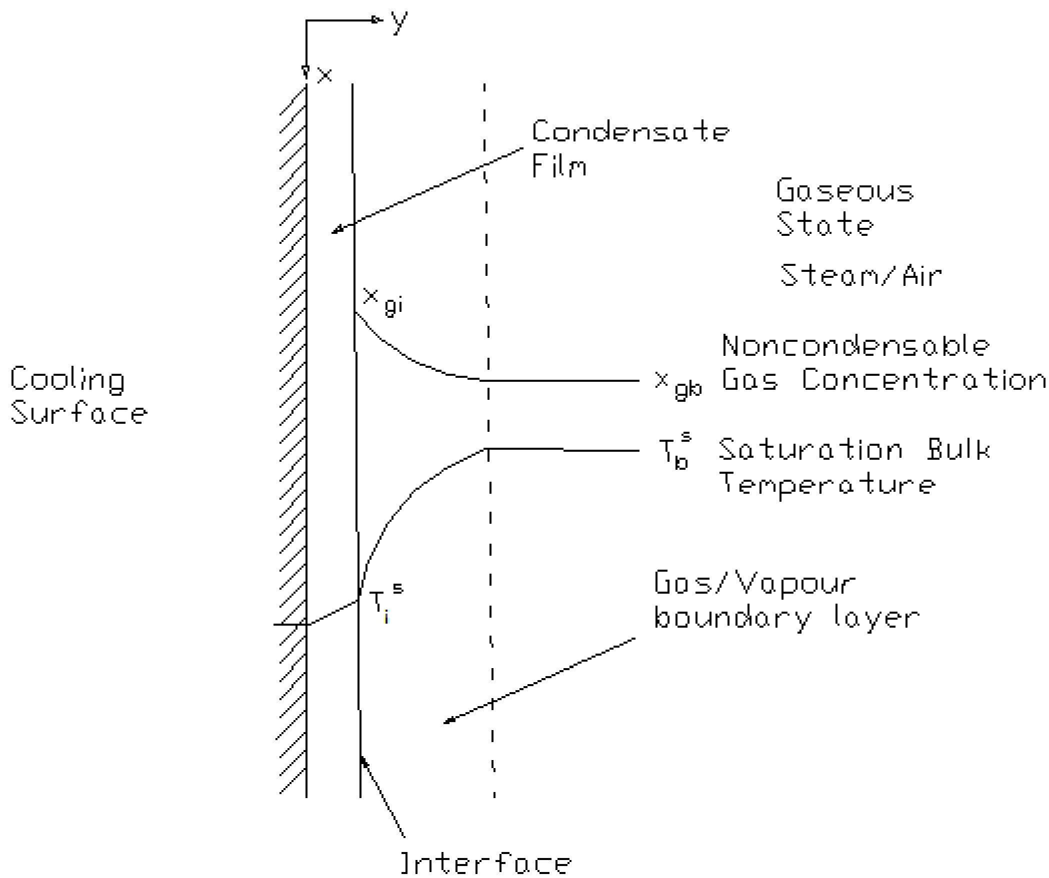

Figure 2-3: Boundary layer look at filmwise condensation w/ noncondensable gas [16]

A complication that is introduced along with noncondensable gases is that the saturation temperature is no longer tied to the absolute pressure of the mixture, but to the partial pressure of the vapor. The partial pressure of the vapor will vary spatially within the diffusion boundary layer and is apt to vary spatially in the bulk mixture due to stratification between the noncondensable gasses and vapor. This poses a significant challenge for experimentation as the saturation temperature can no longer be determined from a single system pressure measurement and instead must be measured locally. This local temperature measurement can then be used to evaluate the saturation pressure (partial pressure of steam), and the local noncondensable gas fraction if the total system pressure is known.

2.2.1 Minkowycz and Sparrow

Minkowycz and Sparrow [17] expanded on Nusselt's analytical solution to account for the presence of noncondensable gas. The work included an evaluation of the influence of interfacial resistance, superheating, and variable fluid properties for condensation of steam with air. Numerical computation was necessary to achieve solutions for the co-existing variable property boundary layer problem. Results of the work were presented as relative fractions of the Nusselt heat flux (as if for pure vapor) for noncondensable mass fraction between 0.1% and 10%. The solutions suggest that even very low concentrations of noncondensable gas lead to dramatic reductions in heat transfer. For instance, an air mass fraction of just 0.1% is shown to reduce the heat flux by as much as 50% from the Nusselt calculated value while a 10% air mass fraction reduces the heat transfer by roughly 90%.

2.3 Containment Condensation Characterization

In the nuclear industry, condensation of steam in the presence of air is of particular interest in containment analysis. Many Gen III reactor designs have adopted various Passive Containment Cooling Systems (PCCS) to prevent over pressurization of containment structures in the event of a Loss of Coolant Accident (LOCA). This is generally achieved by promoting condensation in the containment volume. These large spaces are occupied with air at approximately atmospheric pressure. In the event of a LOCA, the large inventory of air significantly influences condensation rates. Boiling Water Reactors (BWR) such as the ESBWR and SBWR, generally employ passive heat exchangers which flow cool water through tube bundles, condensing steam on the outside surfaces. Pressurized Water Reactors (PWR) such as the AP-1000 and SPWR employ the containment vessel itself as the condensing surface.

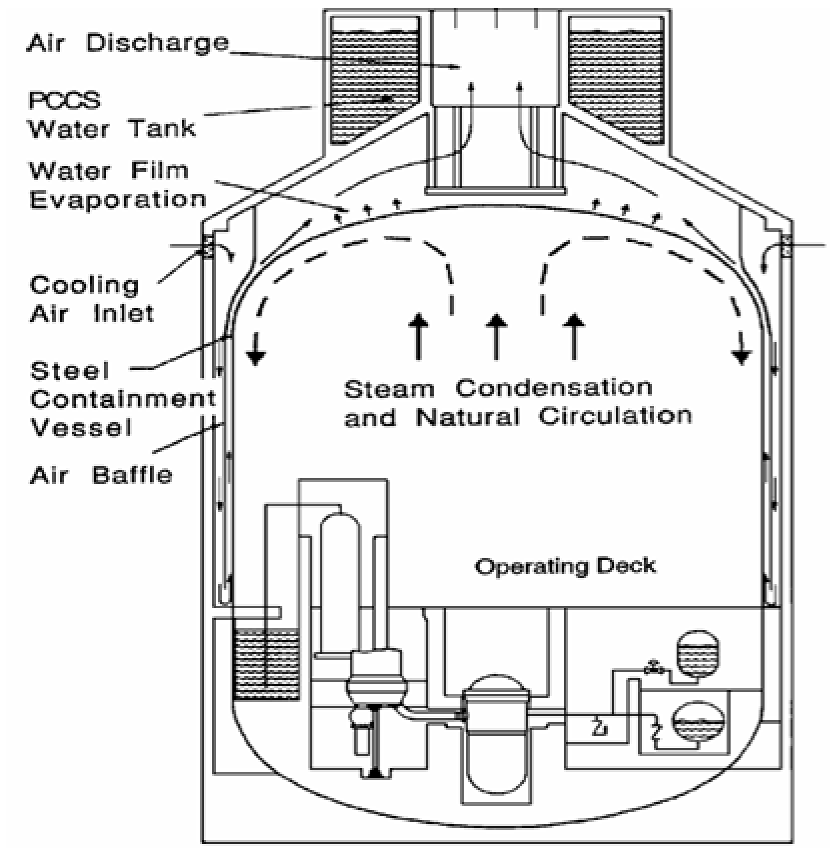

Figure 2-4: Passive Containment Cooling System (PCCS) of the Westinghouse AP600/1000

2.3.1 Uchida and Tagami

Due to the needs of the industry, containment condensation research has generally been focused on quiescent or naturally driven condensation in the presence of large concentrations of noncondensable gas. The most commonly cited work in this area was produced by Uchida [18] and Tagami [19]. Several containment analysis codes (e.g. GOTHIC) directly employ the simple models they proposed.

Uchida and Tagami developed models for evaluating condensation heat transfer coefficients as a function of only the non-condensable mass fraction of a vapor-gas mixture. Both researchers employed the same experimental facility to perform the work. The facility consisted of a containment structure (6.4 meters tall and 3.4 meters in diameter) within which three cooled tubes were employed as condensing surfaces (each 0.3 meters tall and 0.2 meters in diameter). The air mass fraction was varied between 0.1 and 0.95 for the Uchida tests and 0.4 and 0.95 for Tagami's tests. The following is the result of their work:

Uchida:

$$h = 380\left(\frac{\omega_{NC}}{1-\omega_{NC}}\right)^{-0.7}\left[\frac{\mathrm{W}}{\mathrm{m^2K}}\right] \tag{2.6}$$

Tagami:

$$h = 11.4 + 284\frac{1-\omega_{NC}}{\omega_{NC}}\quad\left[\frac{\mathrm{W}}{\mathrm{m^2K}}\right] \tag{2.7}$$

Where ω_{NC} is the mass fraction of non-condensable gas.

While these models are widely employed in predicting containment condensation rates due to their simplicity, many details of the test conditions were not published. Perhaps most importantly, the effects of the velocity field are largely ignored and undocumented, and it has since been shown that this information is necessary for predicting and recreating the results of these tests and others like them. [13]

2.4 The Effect of Steam Pressure on Condensation Rates

During a LOCA or depressurization event, the unique containment of the NuScale Power Module™ is designed to reach pressures on the order of ten times greater than conventional containment designs. Naturally, an improved understanding of the influence of system pressure on condensation rates deserves particular attention for the characterization of these high pressure containments.

The evident effect that steam pressure has on condensation rates is the direct influence on saturation temperature. Saturation temperature increases with steam pressure, providing a greater driving force for heat transfer to a similarly cool surface and improving overall heat transfer rates. This effect provides a feedback response to increasing steam pressure and is of great benefit to condensation systems used to limit over-pressurization. The less well understood influence of steam pressure is on the heat transfer coefficient. In the context of containment condensation, the influence of steam pressure must be evaluated with consideration to the presence of noncondensable gases.

In Nusselt's analytical formulation for pure vapors, condensation heat transfer coefficients are not shown to have a direct dependence on steam pressure. Pressure does however influence the solution through the determination of state properties as well as the degree of wall subcooling (for the same wall temperature, greater steam pressure (i.e. saturation temperature) increases wall subcooling). The result of increased pressure on Nusselt's analysis is actually a slight reduction in heat transfer coefficients.

Minkowycz and Sparrow did not explicitly address the influence of system pressure in their work, however they did note that the attenuating effect of noncondensable gases was greater at reduced saturation temperatures. That is, increasing the steam pressure showed significant improvement in heat transfer coefficients when noncondensable gasses were present. While this result was only demonstrated for a range of sub-atmospheric pressures, this conclusion suggests that system pressure influences the transport processes occurring in the diffusion boundary layer.

2.4.1 Dehbi

Uchida reported in his investigation that condensation heat transfer coefficients were not a function of pressure, local velocities, or molecular weight of the participating gases, yet he presented little substantiation for these claims. To expand upon this work, Dehbi [20] conducted an experimental investigation to evaluate the dependence of condensation rates on additional parameters, including system pressure, wall subcooling, and condensing length.

Similar to the Uchida and Tagami's facility, Dehbi's experimental apparatus consisted of a steam vessel (4.5 meter tall and 0.45 meter diameter) within which a cooled copper tube was employed as a condensing surface (3.5 meter long and 3.8 cm diameter). Steam was generated by a set of heaters immersed in a pool of water at the bottom of the vessel while noncondensable gasses were introduced from the top. The region occupying the condensing surface was subdivided into multiple sections where thermocouples measuring bulk mixture, tube, and coolant temperatures were placed to evaluate axial variation of the heat flux.

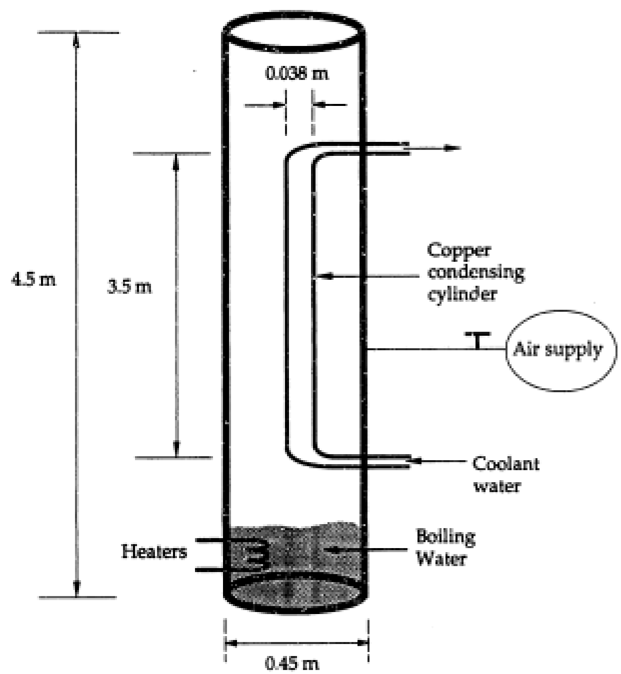

Figure 2-5: Diagram of Dehbi's condensation test facility

Dehbi conducted experiments with air mass fractions ranging from 0.25 to 0.90 at system pressures of 1.5, 3.0, and 4.5 atmospheres. He found that heat transfer rates increased measurably with pressure. Among the outcomes of his work is the following correlation that relates the average heat transfer coefficient along the condensing surface to system pressure, non-condensable mass fraction, and wall subcooling:

Dehbi:

$$\overline{h}_L = \frac{L^{0.05}[(3.7 + 28.7P) - (2438 + 458.3P)\log_{10}\omega]}{\left(\overline{T}_\infty - \overline{T}_w\right)^{0.25}} \quad \left[\frac{\mathrm{W}}{\mathrm{m^2K}}\right] \tag{2.8}$$

Dehbi compares his results to those of Uchida and Tagami and shows relatively good agreement in the magnitude of heat transfer coefficients and effect of noncondensable gas. Dehbi concludes that the Uchida correlation appears conservative for pressures above 2 atmospheres while Tagami's model is conservative across the entire range of pressures evaluated.

Dehbi performed tests with air as well as with a helium-air mixture which helped provide remarks on stratification between the gases and steam. When the helium-air mixture was used, total noncondensable concentrations had to be very large to prevent stratification. When just air, which is heavier than steam, was used, stratification was prevented because the steam source was at the bottom of the vessel which promoted mixing.

2.4.2 Kim

Recently, Kim [21] investigated condensation heat transfer in the presence of non-condensable gas at high pressures (up to 2.0 MPa) for the analysis of the unique steam-gas pressurizer of the conceptual REX-10 reactor. With a cooled tube condensing surface inside of a steam vessel, the experimental apparatus was similar to that used by Dehbi, Uchida, and Tagami (Figure 2-6).

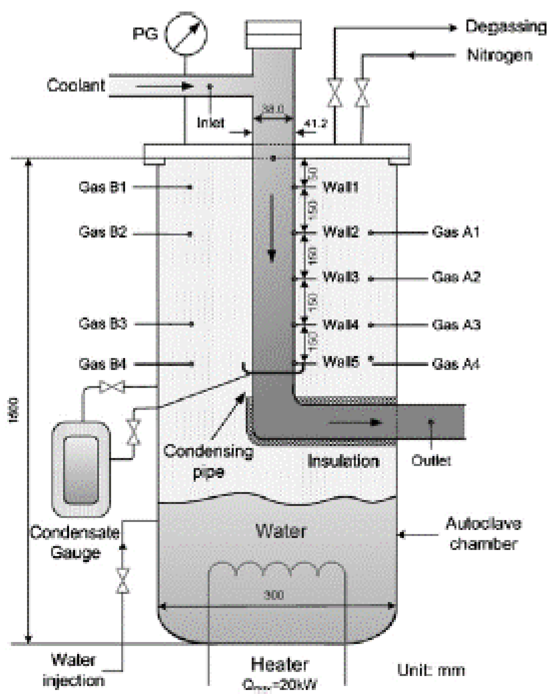

Figure 2-6: Diagram of Kim's condensation test facility

A semi-empirical model based on the mass heat transfer analogy is proposed and shown to correlate well with the experimental data. Comparisons are made with the popular Uchida, Tagami, Dehbi models showing good agreement at low pressures. The main conclusion of the work is that heat transfer coefficients appear to increase significantly with pressure.

2.5 Relevant MASLWR Studies

2.5.1 Jason Casey Thesis

Casey [22] investigated containment condensation in the MASLWR facility for a pair of blowdown tests. These tests involved opening the PCS valves that connect the primary system and the containment and allowing circulation between the two vessels. One test was performed with an evacuated containment and the other was performed with an atmospheric containment. Comparison between the tests show very little influence of the noncondensable gas. Condensation heat transfer coefficients were found to be unusually low when compared to popular models.

2.5.2 Ben Bristol Thesis

Bristol [23] analyzed the data sets described in this thesis. His work is focused on the single phase natural convection heat transfer on the pool side of the heat transfer plate. Bristol describes the experiments in detail and evaluates the mass and energy flows occurring during the tests. His results shows relatively good agreement between the measured and predicted heat transfer coefficients on the pool side.

2.6 Objectives of Current Investigation

The goal of this investigation is characterize the condensation rates in the MALSWR test facility containment. This scaled facility represents a unique opportunity to study condensation in a configuration that closely resembles prototypic SMR designs, notably the NuScale Power Module™.

While there has long been interest in the area of containment condensation, the prior work has been focused on the conditions expected in traditional containment configurations. The most widely applied models for estimating containment condensation rates were developed for modest pressures and large noncondensable gas concentrations. The accident conditions expected in the containment of the NuScale Power Module™ lie far outside the range of applicability of the popular models.

The objective of the experimental work is to quantify the condensation heat flux and heat transfer coefficient on the HTP over a range of containment pressures and initial noncondensable gas inventories. Where applicable, the results are compared to the predictions from popular condensation models. The condensation heat flux and heat transfer coefficients are primarily quantified with the thermocouple measurements in the heat transfer plate. An alternate method based on the condensate level measurement is also proposed and evaluated.

3 Experimental Facility

The OSU MASLWR test facility is a system-level scaled facility developed to demonstrate the feasibility of the prototypic MASLWR concept. The original requirements for the scaled facility were to properly model both the steady-state operation of the MASLWR concept and the integral response to a variety of small-break LOCA transients. Based on these requirements, the following modes of plant operation were to be addressed with the facility: Single and two phase natural circulation, reactor system depressurization, and ensuing containment pressure response.

Informed with the application of the PIRT (Phenomena Identification Ranking Table) process, the rigorous scaling methodology established similarity criteria and evaluated scaling distortions for each of the three plant operating modes discussed above. The result of the scaling analysis was the specification of appropriate test facility dimensions and operating conditions. [24]

Table 3-1: OSU MASLWR test facility scaling [24]

Geometric Parameters	**Scaling Ratio**
Area	1:82.2
Length	1:3.1
Volume	1:254.7
Operating Parameters	
Temperature	1:1
Pressure	1:1
Time	1:1
Power	1:254.7
Mass Flow Rate	1:254.7
Fluid Velocity	1:3.1

An unfortunate consequence of the scaling requirements is the geometric impossibility of conserving both the appropriate volumes and shared surfaces areas of reduced-scale concentric vessels. To resolve this challenge, the scaled RPV, HPC, and cooling pool were constructed as separate vessels with the HPC and cooling pool sharing an external surface (Figure 3-1). The heat transfer area between the containment and the cooling pool, a critical parameter for characterizing containment pressure response and heat removal rate, is modeled with a heat transfer plate that physically mates the two vessels. While conduction through the RPV into the containment can be an important heat transfer pathway in the prototypic design, it is not evaluated with this facility.

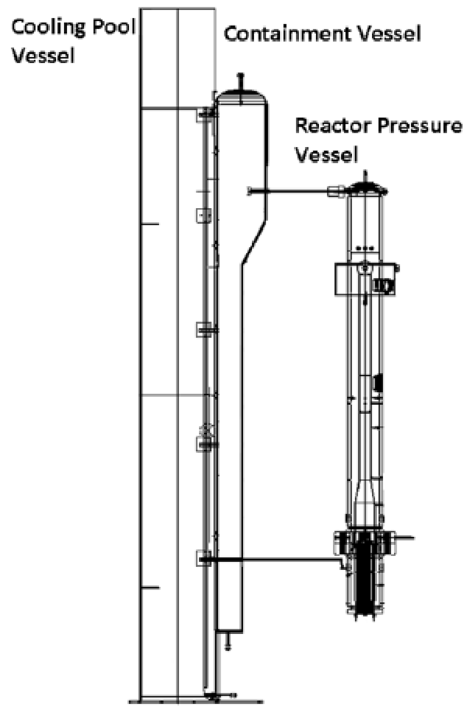

Figure 3-1: Diagram of the OSU MASLWR test facility [25]

The experiments conducted for the investigation outlined in this thesis were limited primarily to the containment vessel and cooling pool of the MASLWR test facility. The description of the experimental apparatus will thus be focused on those related systems.

3.1 High Pressure Containment

The MASLWR facility containment vessel, termed the High Pressure Containment (HPC), is a tall and narrow stainless steel vessel standing at a height of 5.75 meters with a lower and upper diameter of 27 cm and 51 cm respectively. The vessel was constructed in three shells with a conical frustum joining the lower and upper segments. A flat plate and a torispherical head seal the lower and upper ends of the vessel. Due to the scaling requirements of the containment, only a portion of the vessel's external surface may conduct heat to the cooling pool. A flat surface subtends the otherwise circular cross section along the entire height of the containment to accommodate mating between the vessels with the scaled heat transfer plate (Figure 3-3). The other surfaces of the HPC maintain a near-adiabatic condition with 10 cm of calcium silicate insulation and the optional use of three banks of strip heaters to maintain saturation conditions on the wall.

Thermocouples are available in various locations within the HPC to provide information on the temperature distribution within the containment. These include a measurement for the steam bulk at the top of the containment (TF802) and a measurement for the condensate pool temperature (TF804). Thermocouples placed just off the surface of the heat transfer plate measure temperatures within the condensation boundary layers (TF821 through TF861). Several thermocouples measure the HPC vessel surface on the insulated sides of the containment (TW892 through TW894) and on the containment strip heaters (TH892-TH894).

System pressure is measured at the top of the containment relative to ambient pressure (PT801). The liquid level of the condensate is measured with a level differential pressure meter (LDP801). The level is based on a pressure differential between the top and bottom of the containment, equating to the hydrostatic head of the condensate pool. A standard density of water is used to convert to a length scale. [26]

3.2 Heat Transfer Plate

The heat transfer plate (HTP) mates the HPC and cooling pool which, as scaled, represents the entire outside surface area of the prototypic MASLWR containments. As per the scaling requirements, the heat transfer plate in the MASLWR facility shares many parameters of the prototypic vessel. The balance between the convective and conductive heat transfer resistances must be maintained to replicate the spatial temperature response of the containment wall. Additionally, the thermal capacitance (tendency to absorb heat) must be conserved. As such, the HTP was designed with the same material and thickness of the prototypic containment wall [24]. Made of stainless steel type 316L, the HTP is 3.81 cm thick, 16.84 cm wide, and 5.65 meters tall, spanning all but the upper head of the containment vessel.

The heat flux across the plate is quantified via a temperature gradient as measured from an array of embedded thermocouples. At 6 elevations along the height of the plate (i=1 through 6), thermocouples are embedded on the HPC side (TW8i2), the midline (TW8i3), and the CPV side (TW8i4) of the HTP. A conductive heat flux can be evaluated with the temperature gradient measured between the surfaces.

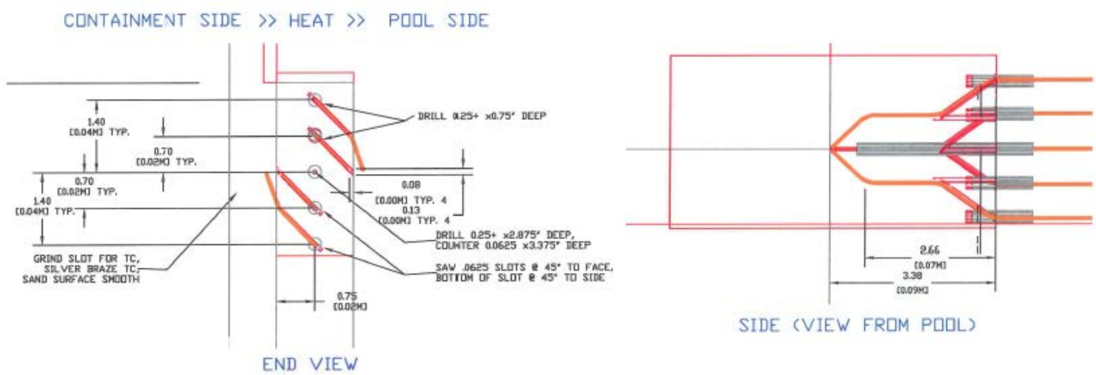

Figure 3-2: Diagram of HTP embedded thermocouples

3.3 Cooling Pool Vessel

Across the HTP from the containment lies the cooling pool vessel (CPV), modeling the open pool in which the prototypic MASLWR containment is submerged. The CPV is taller than the HPC at 7.37 meters with an outside diameter of 76.84 cm and thickness of 0.635 cm. The CPV is insulted with 5 cm of calcium silicate. Thermocouples are employed to measure bulk temperature in the upper regions of the cooling pool (TF901 through TF903). A level differential pressure meter measures the level (LDP901). [26]

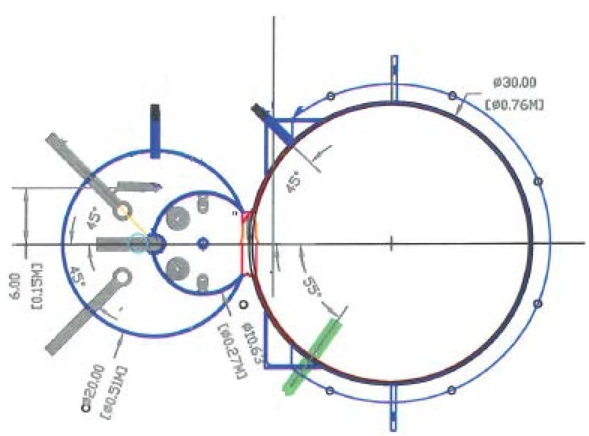

Figure 3-3: Cross-sectional view of the HPC (left) and CPV (right), joined by the HTP.

3.4 Steam Supply System

To support this investigation, a modification was made to the steam supply system of the MASLWR test facility. For these tests, the primary side of the MASLWR facility was operated at reduced power to produce steam with the steam generator. The steam outlet piping, which normally exhausts to the environment, was modified to tap into the Automatic Depressurization System (ADS) penetrations on the containment. A set of remotely controlled valves allows the redirection of flow on command. The rate of steam supply was controlled by managing the feed flow pump as well as the core power.

The secondary circuit is pressurized throughout the tests. Choking of the flow between the steam generator and the containment occurs at the pressure regulating valve upstream of the modified steam piping. The inlet steam pressure is assumed to be at the HPC pressure (PT801) and the steam temperature is measured in the ADS penetration (TF873A). The flow rate is quantified with a magnetic flow meter in the feed flow line (FMM501).

3.5 Facility P&ID

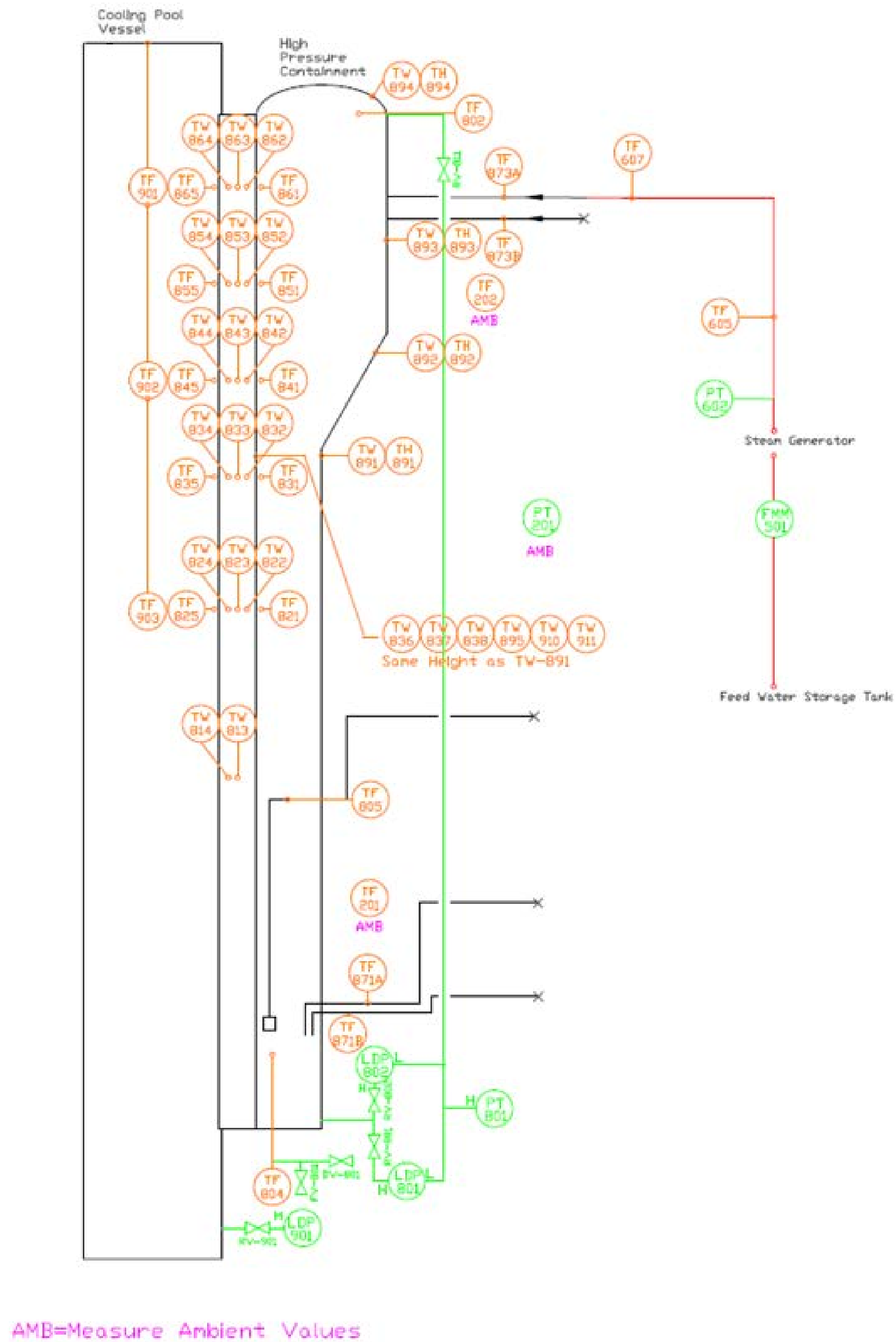

Figure 3-4: P&ID of relevant instruments of the OSU MASLWR test facility.

The P&ID diagram shown in Figure 3-4 describes the placement of instruments in the HPC, HTP, and CPV. Table 3-2 contains the elevations of important thermocouple measurements relative to the bottom of the HPC.

Table 3-2: Elevation of relevant facility thermocouples

Instrument	Elevation (m)	Location
TF873A	4.68	Steam inlet
TF802	~5.60	Upper steam bulk
TF804	~0.50	Condensate pool
TW/TF81X	1.00	HTP
TW/TF82X	2.50	HTP
TW/TF83X	3.20	HTP
TW/TF84X	4.10	HTP
TW/TF85X	5.10	HTP
TW/TF86X	5.60	HTP
TW/TH891	3.27	HPC insulated surface
TW/TH892	4.13	HPC insulated surface
TW/TH893	5.15	HPC insulated surface
TW/TH894	5.66	HPC insulated surface
TF901	5.60	CPV bulk
TF902	4.10	CPV bulk
TF903	2.50	CPV bulk

3.6 Facility Limitations

The MASLWR test facility provides a unique opportunity to evaluate condensation rates in an SMR containment configuration. However, experimental research into containment condensation has generally been performed with specifically designed separate effects facilities. These facilities allow for the purposeful placement of instrumentation and precise control of boundary conditions that cannot be accomplished with the MASLWR facility. This facility was developed to broadly demonstrate the feasibility of the MASWLR concept. Since the conclusion of the original scope of work, use of the facility has been extended into testing it was not specifically designed for.

NuScale has adopted two design changes relevant to the topic of this thesis since the construction of the original MASLWR facility. One of these changes is the adoption of a ‘dry’ containment. The containment of the MASLWR concept is partially filled with water during operation. When the ECCS is actuated, the primary coolant from the RPV is sparged into the pool to provide pressure suppression. In the present NuScale design, the containment is dry and maintained at a deep vacuum. This removes the need for insulation and provides other benefits, however the peak pressures expected following an ECCS actuation are much higher.

To accommodate the design change, MASLWR testing has since been performed with a dry containment. While the facility can function in this manner, the instrumentation in the HPC is not well arranged to characterize condensation occurring on the lower half of the plate as this region was designed to be submerged. Additionally, the sole thermocouple set representing the bottom portion of the plate has since been partially damaged.

The second design change is a significant increase in the primary coolant operating pressure. In addition to the dry containment, these two changes increase peak containment pressure several times over the MALSWR concept. While the facility was scaled to operate at the temperatures and pressures of the original concept, the facility is not designed to handle the increased pressure of the present NuScale design. As such, this investigation is limited to evaluating condensation at relatively moderate pressures (~21 bar). The same tests will be performed with the renovated facility across the full range of prototypic pressures. [23]

Other limitations of the facility include a lack of bulk temperature measurements along the height of the containment. These temperature measurements are necessary for quantifying local noncondensable gas concentrations. Assumptions must be made as to the mixing of the noncondensables as well as to the state of the steam (superheated vs. saturated).

Another limitation is that the cooling pool heat sink increases substantially in temperature during the course of test, influencing overall heat transfer rates. This is particularly problematic in longer tests. In addition, the available condensation area on the heat transfer plate continuously decreases over the course of a test as the condensate level rises. These limitations make it difficult to maintain steady state conditions.

4 Methods

4.1 Test Procedure

A series of tests were devised to characterize the condensation rates in the MASLWR containment. The objective of these tests was to achieve, in a controlled manner, high steam pressure in the containment vessel while measuring the condensation rate occurring along the heat transfer plate.

4.1.1 Test Set 1

Steam for these tests was produced in the steam generator while operating the MALSWR facility at steady-state. The detailed startup procedure involved slowly raising the RPV pressure and temperature with use of the pressurizer and core heaters. For the first round of testing, the core power was raised to either 10% or 20% of nominal operating power, 40 kW and 80 kW respectively. Secondary flow through the steam generator was initiated during the heat-up to promote natural circulation in the primary loop. The secondary flow was eventually increased until it was removing the entirety of the heat being supplied with the heaters. Appropriate control of the secondary was important for achieving steady operation and was performed with the feed flow pump and the steam pressure regulating valve. The primary system was allowed to reach steady state as indicated by stable flow rates and fluid temperatures along the primary loop. Steam being generated at this stage was exhausted to the environment.

Prior to introducing steam into the containment, the desired initial air inventory in the containment was achieved with use of a vacuum pump. For the first round of tests, the containment was evacuated to either a ‘near-vacuum’ condition, ‘half-vacuum’ condition, or left at atmospheric pressure. At roughly 1 psia or 0.07 bar, the near vacuum condition was the lowest pressure that could be achieved with the containment vacuum pump.

For the first set of tests, it was decided that preheat would be used to mitigate the thermal inertia of the HPC surface. After evacuating the containment to the desired pressure, the three banks of heaters were set achieve a wall temperature of approximately 160°C, corresponding to a saturation pressure of about 6 bar. The heaters were turned off at the initiation of the tests to avoid energy balance complications.

Once the pre-test checklist had been completed, the tests were initiated by redirecting steam from the normal outlet to the modified steam piping which taps into the containment. For the first round of tests, the steam pressure was maintained at approximately 21 bar in the secondary. Strip heating was employed to maintain saturation conditions on the surface of the piping to prevent condensation upstream of the containment.

The first round of tests involved introducing a constant rate of steam into the containment until either the containment approached its design pressure of almost 21 bar or a predetermined time of 90 minutes had elapsed. The rate of steam being supplied to the containment was equal to the rate of steam being generated in the secondary, equivalent to either 40 kW or 80 kW of core power depending on the test. Once the termination conditions for the tests were met, the steam supply was directed back to the normal steam path and the containment was allowed to depressurize naturally from condensation. For the first two tests performed (Test 1.1 and Test 1.2), steam was redirected back into the containment for a second run after 10 minutes of natural depressurization. However, only the first of the two trials is considered in this thesis. When testing was complete for the day, the RPV was depressurized and allowed to cool down.

Table 4-1: Test matrix for first set of condensation tests

Air Pressure:	*0.07 bar*	*0.5 bar*	*1.0 bar*
40 kW	Test 1.1	Test 1.3	Test 1.5
80 kW	Test 1.2	Test 1.4	Test 1.6

4.1.2 Test Set 2

The first tests were performed such that the containment pressure and temperature were continually increasing throughout the testing period which may have introduced transient effects that cannot easily be accounted for. The MASLWR facility was not designed to support the type of steady state conditions that would be desirable for these containment condensation experiments. Nevertheless, a second set of tests were devised to mitigate transient effects and generally improve test conditions. The objective for these tests was to achieve a period of stable or even slightly decreasing containment pressure. The results would help determine if the continuously increasing temperatures and pressures from the first tests were influencing the observed trends in condensation rates.

The second set of tests were conducted by quickly ramping up the containment pressure and then reducing the flow rate of steam into the vessel so as to roughly match the rate of condensation on the heat transfer plate. Each test was designed to achieve and maintain (for a short period of time) a unique steam pressure. To ramp-up pressure in the containment at the beginning of each test, the core power was set to 120 kW with an appropriate feed flow rate. Calculations were made beforehand for each test to determine a ‘ramp-up time’ as well as a reduced core power and feed flow rate estimated to roughly match the condensation rate on the heat transfer plate. Containment pressure eventually began to increase again. This is because, as the tests progress, the exposed condensation surface area decreases and the heat sink warms up. These tests were terminated once 30 minutes had elapsed since the initial steam injection. Containment strip heating was not employed with these tests to simplify the energy accounting.

While performing a scoping run of these tests, it was found that flow instabilities occurred once the steam flow rate was reduced. The instability was determined to be related to choking of the flow into the containment. To avoid this, the steam drum pressures were reduced such that they were less than twice the target containment pressure for each test.

Table 4-2: Test matrix for second set of condensation tests

	Initial Pressure	*Steam Drum Pressure*	*Ramp-Up Time*	*Reduced Power*	*Reduced Feed Flow (kg/s)*
Test 2.1	Near-Vacuum	5.17 bar	4 minutes	44 kW	0.0139
Test 2.2	Near-Vacuum	10.34 bar	6 minutes	52 kW	0.0164
Test 2.3	Near-Vacuum	17.24 bar	8 minutes	60 kW	0.0189
Test 2.4	Near-Vacuum	20.68 bar	10 minutes	68 kW	0.0215
Test 2.5	Atmospheric	10.34 bar	3 minutes	40 kW	0.0126
Test 2.6	Atmospheric	13.79 bar	5 minutes	48 kW	0.0151
Test 2.7	Atmospheric	20.68 bar	7 minutes	56 kW	0.0177

4.2 Data Processing and Analysis

The data analysis presented in this thesis comprises the necessary calculations to quantify condensation rates, condensation heat fluxes, and heat transfer coefficients in the HPC for the 13 tests listed above. A mass and energy balance is included to evaluate the quantification methods employed. The data collected from the tests was imported and organized into EXCEL spreadsheets and read into the MATLAB coding environment where the calculations were performed.

4.2.1 Assumptions

The following assumptions were made to permit meaningful analysis of the test data.

1 The HPC and CPV are well insulated and environmental heat losses are assumed to be negligible. This assumption is justified from the results of the energy balance in section 5.4 of this report.

2 Steam entering the containment is assumed to be superheated at the containment pressure (PT801) and the temperature measured in the ADS line (TF873A). If the flow is choked, it is occurring at the steam pressure regulating valve, well upstream of the containment and ADS line.

3 The steam bulk in the HPC is assumed to be at saturation conditions during the course of the tests. This assumption is corroborated with wall temperature measurements at various locations. The noncondensable gases are assumed to be at the same temperature as the vapor. After termination of the steam flow into the containment, the ensuing depressurization leads to significant superheat (in regions not adjacent to the HTP) which is sustained in part by the thermal inertia of the structures.

4 Noncondensable gases and steam do not mix and are assumed to segregate completely within the HPC. This formidable assumption was developed in review of the test results and is justified in the section 5.6. Complete segregation between the gasses may not be entirely realistic, however the test results clearly indicate strong stratification with noncondensable gases concentrated at the bottom of the containment. This simplifying assumption implies that the partial pressures of steam and air are both equal to the system pressure in the regions of the HPC that they respectively occupy.

5 The temperature of the condensate pool at the bottom of the containment is measured with TF804. This thermocouple is elevated roughly half a meter from the bottom of the containment. During the initial period of each test, this thermocouple is measuring gas and vapor temperatures until becoming submerged in the condensate pool. To account for this, the condensate temperature and thermal properties are evaluated at saturation unless TF804 reads subcooled temperatures.

6 Due to a lack of temperature instrumentation in the bottom portion of the CPV, the bulk temperature along the entire height of the pool is extrapolated from three temperature measurements available in the top half of the vessel (TF903, TF902, and TF901). A linear least-squares fit is employed for this purpose. The result of this extrapolation is discussed in section 5.4 of this report.

7 The heat flux through the HTP is evaluated using Fourier's Law. This involves an assumption of steady state (i.e. negligible heat capacitance) and 1-D conduction. The validity these assumptions are addressed in section 5.4 and 6.2 of this report.

8 Material and thermal properties for air and the SS316 HTP are assumed constant and independent of changing temperature and pressure.

4.2.2 Data Channels

The following instrument data channels were employed in the data analysis. Test facility data was collected at 1 second intervals.

Table 4-3: Test facility instrument channels employed in the analysis

Channel	**Description**	**Unit**
High Pressure Containment		
FMM501	Steam flow rate	lbm/min
PT801	HPC gauge pressure (relative to ambient pressure)	psig
LDP801	HPC liquid level	in
TF802	HPC upper dome temperature	°F
TF804	HPC condensate pool temperature	°F
TF873A	HPC steam inlet temperature	°F
Heat Transfer Plate		
TW813	Centerline HTP temperature	°F
TW814	CPV side HTP surface temperature	°F
TW822	HPC side HTP surface temperature	°F
TW823	Centerline HTP temperature	°F
TW824	CPV side HTP surface temperature	°F
TW832	HPC side HTP surface temperature	°F
TW833	Centerline HTP temperature	°F
TW834	CPV side HTP surface temperature	°F
TW842	HPC side HTP surface temperature	°F
TW843	Centerline HTP temperature	°F
TW844	CPV side HTP surface temperature	°F
TW852	HPC side HTP surface temperature	°F
TW853	Centerline HTP temperature	°F
TW854	CPV side HTP surface temperature	°F
TW862	HPC side HTP surface temperature	°F
TW863	Centerline HTP temperature	°F
TW864	CPV side HTP surface temperature	°F
Cooling Pool Vessel		
LDP901	CPV liquid level	in
TF901	CPV temperature	°F
TF902	CPV temperature	°F
TF903	CPV temperature	°F

The data channels are identified with the same alphanumeric label in all of the calculations presented and throughout this thesis.

4.2.3 Input Parameters

In addition to the instrument data channels, the following input parameters were used for the data analysis.

Table 4-4: Input parameters employed in the analysis

Parameter	Value	Variable
High Pressure Containment		
Cross sectional area of lower HPC	0.0539 m^2	A_{HPC}
Total volume of HPC	0.5174 m^3	V_{HPC}
Heat Transfer Plate		
Width of HTP	0.1682 m	W_{HTP}
Thickness of HTP	0.0381 m	Th_{HTP}
Height of HTP	5.645 m	H_{HTP}
HTP elevation of 81X (relative to bottom of HTP)	1.00 m	--
HTP height for 81X	1.75 m	H_{81X}
HTP elevation of 82X	2.50 m	--
HTP height for 82X	1.10 m	H_{82X}
HTP elevation of 83X	3.20 m	--
HTP height for 83X	0.80 m	H_{83X}
HTP elevation of 84X	4.10 m	--
HTP height for 84X	0.95 m	H_{84X}
HTP elevation of 85X	5.10 m	--
HTP height for 85X	0.75 m	H_{85X}
HTP elevation of 86X	5.60 m	--
HTP height for 86X	0.295 m	H_{86X}
Cooling Pool Vessel		
Cross sectional area of CPV	0.4410 m^2	A_{CPV}
CPV elevation of TF903 (relative to bottom of CPV)	3.21 m	El_{903}
CPV elevation of TF902	4.81 m	El_{904}
CPV elevation of TF901	6.31 m	El_{905}
Average CPV pressure	1.3 bar	P_{CPV}
Material and Thermal Properties		
c_p for air (assumed constant, evaluated @120°C)	1.013 kJ/(kg-K)	Cp_{air}
c_p for HTP (SS316, assumed constant)	0.50 kJ/(kg-K)	Cp_{HTP}
k-thermal conductivity for HTP (assumed constant)	16.3 W/(m-K)	k_{HTP}
Density of HTP	8000 kg/m^3	ρ_{HTP}
Standard temperature for LDP measurements	4°C	T_{STD}
Standard pressure for LDP measurements	1.01325 bar	P_{STD}

4.2.4 Data Manipulations

This section presents the data manipulations required to form the quantities used in the calculations of the mass and energy balance, as well as the condensation characterization.

MATLAB based XSteam functions were employed to evaluate steam and liquid water properties as a function of pressure and temperature at each data point throughout the tests. The properties evaluated are saturation temperatures, densities, and specific enthalpies and internal energies. For superheated steam or subcooled liquid, properties are evaluated as a function of pressure and enthalpy. When the fluid is saturated, the phase is specified (either *l* or *v*) along with the pressure. Saturation temperature does not require a phase specification.

The data imported into the MATLAB environment was converted to S.I. units. Units were chosen for compatibility with the XSteam steam table script. Pressures were converted to bar, temperatures were converted to °C, levels were converted to meters, and the steam flow rate was converted to kg/s.

The HPC liquid level measurement, LDP801 is based off of a pressure differential measured between the top and bottom of the containment equivalent to the hydrostatic head of the condensate pool (the hydrostatic head of the vapor component is neglected). The data acquisition system internally converts this pressure measurement to a liquid level assuming a liquid density at standard conditions of 4°C and 1.10325 bar. When importing the instrument data into MATLAB, the value for LDP801 was adjusted for the appropriate liquid density based on the temperature of TF804. Additionally, an adjustment to the channel was required to output a positively increasing value starting at 0 meters whereas the original channel output a negative value which tended toward 0 as the liquid level increased.

$$LDP801_{adjusted}(:) = [LDP801_{raw}(:) - LDP801_{raw}(1)] \cdot \frac{\rho(P_{STD}, T_{STD})}{\mathbf{max}\left[\rho(PT801, TF804), \rho_{sat,l}(PT801)\right]} \tag{4.1}$$

TF804 initially measures gas and vapor temperatures in the containment until becoming submerged in the condensate pool. To avoid occasionally calculating steam densities (TF804 will hang around the saturation line until submerged), the saturated liquid density is used unless the measured temperature is subcooled (Assumption 5).

The HPC pressure measurement, PT801, was adjusted to provide absolute pressure as opposed to gauge pressure.

$$PT801_{adjusted} = PT801_{raw} + P_{STD} \tag{4.2}$$

These adjustments were performed after converting to S.I. units.

4.2.4.1 *Condensate Pool Quantities*

Volume of condensate pool:

$$V_{liq} = LDP801 \cdot A_{HPC} \tag{4.3}$$

Mass of condensate pool:

$$m_{liq} = V_{liq} \cdot \mathbf{max}[\rho(PT801, TF804), \rho_{sat,l}(PT801)] \tag{4.4}$$

TF804 initially measures gas and vapor temperatures in the containment until becoming submerged in the condensate pool. To avoid occasionally calculating steam densities (TF804 will ride the saturation line until submerged), the saturated liquid density is used unless the measured temperature is subcooled.

Internal energy of condensate pool:

$$E_{liq} = m_{liq} \cdot \mathbf{min}[u(PT801, TF804), u_{sat,l}(PT801)] \tag{4.5}$$

The same reasoning applies as the above comment for employing the minimum of the two specific energies.

4.2.4.2 *Noncondensable Gas Quantities*

Mass of noncondensable gas:

$$m_{NCG} = \frac{PT801_{initial} \cdot V_{HPC} \cdot \; MW_{air}}{\bar{R} \cdot (TF802 + TF804)_{inital}/2} \tag{4.6}$$

The total mass of noncondensable gas in the containment remains unchanged along the course of each test. The mass is calculated using ideal gas relations. The containment pressure and average temperature used in the calculation are measured prior to preheating of the containment (in units of Pa and K respectively).

Volume of noncondensable gas:

$$V_{NCG} = \frac{m_{NCG} \cdot \overline{R} \cdot T_{sat}(PT801)}{PT801 \cdot MW_{air}} \tag{4.7}$$

As per Assumption 4, the noncondensable gas and vapor are assumed to occupy distinct spaces in the containment with the noncondensable gas concentrated at the bottom. Pressure and temperature are evaluated in units of Pa and K respectively.

Internal energy of noncondensable gas:

$$E_{NCG} = m_{NCG} \cdot \ Cp_{air} \cdot T_{sat}(PT801) \tag{4.8}$$

4.2.4.3 *Vapor Quantities*

Volume of vapor:

$$V_{vap} = V_{HPC} - V_{liq} - V_{NCG} \tag{4.9}$$

The volume of vapor in the containment is taken as the entire volume of the HPC less the space occupied by the condensate and noncondensable gas (see Assumption 4).

Mass of vapor:

$$m_{vap} = \rho_{sat,v}(PT801) \cdot V_{vap} \tag{4.10}$$

Internal energy of vapor:

$$E_{vap} = m_{vap} \cdot h_{sat,v}(PT801) \tag{4.11}$$

4.2.4.4 Steam Flow and Phase Change Quantities

Integral steam mass flow into HPC:

$$m_{stm,in} = \sum_{i=LB}^{RB} FMM501(i) \cdot dt \tag{4.12}$$

The integrated steam flow at any time along the course of the test is the cumulative sum of the flow rate times the data collection frequency. The frequency, *dt*, is equal to 1 second for all of the calculations. The terms *LB* and *RB* refer to the left and right bounds of the period of interest for each test.

Steam enthalpy flow rate into HPC:

$$\dot{H}_{stm,in} = FMM501 \cdot h(PT801, TF873A) \tag{4.13}$$

Integral enthalpy flow into HPC:

$$H_{stm,in} = \sum_{i=LB}^{RB} \dot{H}_{stm,in}(i) \cdot dt \tag{4.14}$$

Heat removed from inlet steam to become subcooled condensate (primarily latent heat):

$$E_{phase} = m_{liq} \cdot (h(PT801, TF873A) - \mathbf{min}[h(PT801, TF804), h_{sat,l}(PT801)]) \tag{4.15}$$

This calculation also incorporates the sensible heat removed from the superheated steam and the heat removed to subcooled the condensate.

Sensible heat removed from inlet steam to become bulk saturated vapor:

$$E_{sens} = m_{vap} \cdot (h(PT801, TF873A) - h_{sat,v}(PT801)) \tag{4.16}$$

As per Assumption 3, the vapor and noncondensable gas in the containment is assumed to be at saturation temperature. The sensible heat removed from the superheated inlet vapor must be accounted for in the energy balance.

4.2.4.5 <u>Heat Transfer Plate Quantities</u>

Mass of the HTP:

$$m_{HTP} = \rho_{HTP} \cdot W_{HTP} \cdot Th_{HTP} \cdot H_{HTP} \tag{4.17}$$

Average temperature of the HTP:

$$Tavg_{HTP} = \sum_{i=1}^{6} [TW8i3 \cdot \frac{H_{8iX}}{H_{HTP}}] \tag{4.18}$$

The centerline HTP temperatures are used to evaluate the average temperate of the plate. The plate is discretized into 6 sections centered on the 6 HTP thermocouple sets. The temperatures are weighted by the height of the sections they represent.

Internal energy of the HTP:

$$E_{HTP} = m_{HTP} \cdot \ Cp_{HTP} \cdot Tavg_{HTP} \tag{4.19}$$

Conductive heat flux through the lower HTP:

$$\dot{Q}"_{81X} = k_{HTP} \cdot \frac{(TW813 - TW814)}{Th_{HTP}/2} \tag{4.20}$$

The HTP 81X thermocouple set was damaged before this testing took place. The HPC side surface thermocouple is not available, so the temperature gradient for the lower HTP must be evaluated between the centerline and the CPV surface.

Conductive heat flux through the rest of the HTP:

$$\dot{Q}"_{8iX} = k_{HTP} \cdot \frac{(TW8i2 - TW8i4)}{Th_{HTP}} \tag{4.21}$$

Where i = 2 through 6

As per Assumption 7, the heat flux through the HTP is calculated with neglect of the thermal capacitance of the plate. This is justified as acceptable due to the relatively low thermal storage rate of the HTP when compared to the conduction through the plate (as shown in the energy balance).

Average conductive heat flux through the HTP:

$$\dot{Q}"_{HTP} = \sum_{i=1}^{6}[Q"_{8iX} \cdot \frac{H_{8iX}}{H_{HTP}}] \tag{4.22}$$

Conductive heat rate through the HTP:

$$\dot{Q}_{HTP} = \dot{Q}"_{HTP} \cdot H_{HTP} \cdot W_{HTP} \tag{4.23}$$

Integral conduction through the HTP:

$$Q_{HTP} = \sum_{i=LB}^{RB} \dot{Q}_{HTP}(i) \cdot dt \tag{4.24}$$

4.2.4.6 Cooling Pool Quantities

Average CPV Temperature:

$$T_{CPV} = extrapolated\ from\ TF903, TF902, TF901 \tag{4.25}$$

As per Assumption 6, the temperature along the entire height of the CPV was extrapolated from the three temperatures measured in the upper portion of the pool. A linear relationship was fit to TF901, TF 902, and TF903 at the corresponding elevations El_{901}, El_{902}, and El_{903} using a least-squares method. A second degree polynomial fit was also tried, however this generated non-physical temperature profiles (i.e. getting warmer at the very bottom). Even with added constraints on the polynomial fit, it was decided that a linear fit was a more defensible choice and likely was more physical. The average temperature along the full length of the pool was evaluated by integrating the extrapolated fit. These manipulations were performed with built-in MATLAB functions.

Internal Energy of CPV:

$$E_{CPV} = A_{CPV} \cdot LDP901 \cdot \rho(P_{CPV}, T_{CPV}) \cdot u(P_{CPV}, T_{CPV}) \tag{4.26}$$

4.2.5 Mass balance

A mass balance evaluation is necessary to validate the mass quantification methods employed in the analysis. To perform the mass balance, the steam mass flow into the HPC must be compared to the calculated mass of condensate and steam in the HPC. While it may be logical to compare the measured steam flow rate from the secondary circuit to the instantaneous rate of change of the vapor and condensate mass in the HPC, a comparison of the integrated flows reduces the 'noise' of those measurements and provides a more meaningful result.

To perform the mass balance, the calculated mass of condensate and vapor in the HPC are added together and compared with the integration of the steam flow across the chosen region of interest. To account for the accumulation of mass prior to the period of interest, the effective change in measured mass is evaluated.

$$\Delta m_{liq} = m_{liq}(LB{:}RB) - m_{liq}(LB) \tag{4.27}$$

$$\Delta m_{vap} = m_{vap}(LB{:}RB) - m_{vap}(LB) \tag{4.28}$$

$$\Delta m_{l+v} = \Delta m_{liq} + \Delta m_{vap} \tag{4.29}$$

$$\Delta m_{stm,in} = m_{stm,in}(LB{:}RB) - m_{stm,in}(LB) \tag{4.30}$$

Where *LB* and *RB* are the left and right bounds of the region of interest. Of course, the bounds must be selected such that the steam flow is directed into the HPC during the entire region of interest.

$$\Delta m_{error} = \Delta m_{l+v} - \Delta m_{stm,in} \tag{4.31}$$

$$\%m_{error} = \frac{\Delta m_{error}}{\Delta m_{stm,in}} \cdot 100 \tag{4.32}$$

A mass error calculation gives insight into the accuracy of the various mass measurement methods and the validity of the associated simplifying assumptions. A positive mass error implies a ‘gain’ in system mass. That is, more mass is measured in the HTP than is measured entering the HTP from the secondary circuit.

The definition of ‘error’ should not be equated to traditional instrument or measurement uncertainties. Due to the simplifying assumptions employed in this analysis, the measurement uncertainty associated with the calculated quantities is hard to evaluate meaningfully. Comparing the mass and energy flow calculations provides a more useful evaluation of the accuracy and validity measurements. Admittedly, only limited confidence can be applied to any result as no measurement in the facility is known to be exact.

4.2.6 Energy Balance

To account for the entirety of the energy inputs to the various components of the system, the following quantities must be evaluated and compared:

- Enthalpy of steam into the HPC, $H_{stm,in}$
- Enthalpy of phase change, E_{phase}
- Sensible heat removed from vapor, E_{sens}
- Internal energy of vapor, E_{vap}
- Internal energy of condensate, E_{liq}
- Internal energy of noncondensable gas, E_{NCG}
- Internal energy of the cooling pool, E_{CPV}
- Internal energy of the HTP, E_{HTP}
- Integrated conduction through the HTP, Q_{HTP}

As with the mass balance, all of the aforementioned quantities employed in the energy balance are integral quantities. Comparing the integral quantities greatly reduces noise when compared to comparison of instantaneous rates of change. The integral energy flows are compared over a defined region of interest.

$$\Delta H_{stm,in} = H_{stm,in}(LB{:}RB) - H_{stm,in}(LB) \tag{4.33}$$

$$\Delta E_{phase} = E_{phase}(LB{:}RB) - E_{phase}(LB) \tag{4.34}$$

$$\Delta E_{sens} = E_{sens}(LB{:}RB) - E_{sens}(LB) \tag{4.35}$$

$$\Delta E_{vap} = E_{vap}(LB{:}RB) - E_{vap}(LB) \tag{4.36}$$

$$\Delta E_{liq} = E_{liq}(LB{:}RB) - E_{liq}(LB) \tag{4.37}$$

$$\Delta E_{NCG} = E_{NCG}(LB{:}RB) - E_{ncg}(LB) \tag{4.38}$$

$$\Delta E_{CPV} = E_{CPV}(LB{:}RB) - E_{CPV}(LB) \tag{4.39}$$

$$\Delta E_{HTP} = E_{HTP}(LB{:}RB) - E_{HTP}(LB) \tag{4.40}$$

$$\Delta Q_{HTP} = Q_{HTP}(LB{:}RB) - Q_{HTP}(LB) \tag{4.41}$$

For presenting the energy balance, it is beneficial to form meaningful groups from the aforementioned terms.

$$\Delta E_{HPC,stored} = \Delta E_{vap} + \Delta E_{liq} + \Delta E_{NCG} \tag{4.42}$$

Equation 4.42 represents the internal energy of the three HPC components.

$$\Delta E_{HPC,removed} = \Delta E_{phase} + \Delta E_{sens} \tag{4.43}$$

Equation 4.43 represents the heat removed from the HPC components. This includes the heat that was removed from the superheated inlet steam to become the subcooled condensate, as well as the heat removed from the superheated inlet steam to become the saturated vapor.

$$\Delta E_{HPC,total} = \Delta E_{HPC,stored} + \Delta E_{HPC.removed} \tag{4.44}$$

Equation 4.44 represents all of the heat that is stored in or has been removed from the HPC. This should equate to the heat supplied to the HPC.

$$\Delta E_{CPV+HTP} = \Delta E_{CPV} + \Delta E_{HTP} \tag{4.45}$$

Equation 4.45 represents the heat added to the CPV and HTP. This should equate to the heat removed from the HPC.

$$\Delta E_{system,stored} = \Delta E_{HPC,stored} + \Delta E_{CPV+HTP} \tag{4.46}$$

Equation 4.46 represents the heat stored in all of the components of the system. This should equate to the heat supplied to the HPC by the inlet steam.

A relative error can be defined for various parts of the system. The heat removed from the HPC and the sum of the total internal energy in the system are compared to the steam inlet flow enthalpy. The change in internal energy of the cooling pool and the integrated conductive heat flux across the plate are compared to the heat removed from the HPC.

$$\Delta E_{error,HPC} = \Delta E_{HPC,total} - \Delta H_{stm,in} \tag{4.47}$$

$$\%E_{error,HPC} = \frac{\Delta E_{error,HPC}}{\Delta H_{stm,in}} \cdot 100 \tag{4.48}$$

$$\Delta E_{error,CPV} = \Delta E_{CPV+HTP} - \Delta E_{HPC,removed} \tag{4.49}$$

$$\%E_{error,CPV} = \frac{\Delta E_{error,CPV}}{\Delta E_{HPC,removed}} \cdot 100 \tag{4.50}$$

$$\Delta Q_{error,HTP} = \Delta Q_{HTP} - \Delta E_{HPC,removed} \tag{4.51}$$

$$\%Q_{error,HTP} = \frac{\Delta Q_{error,HTP}}{\Delta E_{HPC,removed}} \cdot 100 \tag{4.52}$$

$$\Delta E_{error,system} = \Delta E_{system\ stored} - \Delta H_{stm,in} \tag{4.53}$$

$$\%E_{error,system} = \frac{\Delta E_{error,system}}{\Delta H_{stm,in}} \cdot 100 \tag{4.54}$$

The results of the mass and energy balance for each of the tests are presented in the sections 5.3 and 5.4 of this report.

4.2.7 Condensation Rates and the Heat Transfer Coefficient

Developing a mass and energy balance is critical to qualifying the measurement methods employed in this investigation. However, the objective of this thesis is to identify the influence of increasing steam pressure and the presence of noncondensable gas on containment condensation rates. The most suitable method of evaluating condensation rates on the HTP is through the measured heat flux from the temperature gradients measured in the plate. The conduction heat flux through the plate is assumed to be equal to the condensation heat flux, as the sensible heat transfer is relatively small in comparison. The data manipulations necessary for evaluating the conduction heat flux have already been described. The heat flux must simply be plotted against the system pressure to identify a dependence. These plots are presented in the results section for each of the tests conducted.

Of greater interest, though, is the determination of a heat transfer coefficient. A heat transfer coefficient can be evaluated by dividing a known heat flux by the driving force for heat transfer, a temperature difference. In the case of filmwise condensation, as described in section 2 of this report, one might define both a condensation heat transfer coefficient (where $\Delta T=T_{vapor}-T_{film,surface}$) and a film heat transfer coefficient (where $\Delta T=T_{film,surface}-T_{wall}$). However, separating these serial heat transfer resistances generally doesn't present much benefit and can be difficult if not impossible to accomplish experimentally. This investigation aims to evaluate an overall heat transfer coefficient, that is, $\Delta T=T_{vapor}-T_{wall}$. As per Assumption 3, the vapor is assumed to be saturated. The heat transfer coefficients on the HTP are calculated as:

$$h_{8iX} = \frac{\dot{Q}"_{8iX}}{[T_{sat}(PT801) - TW8i2]} \tag{4.55}$$

Where i = 2 through 6 (recall the HPC side surface temperature is unavailable for i =1).

The heat transfer coefficients are presented for each of the conducted tests in the results section of this report. They are plotted against test duration as well as system pressure to evaluate a pressure dependence.

4.2.8 Surface Temperature Correction

Substituting in the evaluation for heat flux, the heat transfer coefficient is shown to be calculated as:

$$h_{8iX} = \frac{k_{HTP} \cdot \frac{(TW8i2 - TW8i4)}{Th_{HTP}}}{[T_{sat}(PT801) - TW8i2]} \tag{4.56}$$

It becomes clear that the calculated heat flux is highly sensitive to the HTP thermocouple measurements, particularly the HPC surface temperature, TW8i2. An imprecise or inaccurate HPC side surface temperature measurement will doubly compound the error in measured heat transfer coefficient. The accuracy of the HTP surface temperatures will be made apparent in the energy balance presented in Section 5.4 of this report.

An alternate method, while somewhat contrived, may also be used to estimate the heat transfer coefficients. This method involves defining a HTP heat flux from the measured condensate accumulation in the HPC.

The condensate formation measurement is slow to change and does not accurately capture changing condensation rates. As such, this method is best applied to Test set 2 where, the condensation rate is expected to remain relatively constant through each quasi steady period.

$$E_{latent} = m_{liq} \cdot (h_{sat,v}(PT801) - h_{sat,l}(PT801)) \tag{4.57}$$

$$\Delta\dot{E}_{latent} = \frac{E_{latent}(RB) - E_{latent}(LB)}{RB - LB} \tag{4.58}$$

$$A_{HTP,unsub} = (H_{HTP} - LDP801(LB:RB)) \cdot W_{HTP} \tag{4.59}$$

$$\dot{Q}"_{latent} = \frac{\Delta \dot{E}_{latent}}{\mathbf{mean}[A_{HPT,unsub}]} \tag{4.60}$$

The above equation produces a single value for the average condensation heat flux during the quasi steady region of interest. The effective ΔT required to produce this heat flux across the plate can then be calculated.

$$\Delta T_{effective} = \frac{\dot{Q}"_{latent} \cdot Th_{HTP}}{k_{HTP}} \tag{4.61}$$

The effective ΔT is then centered upon the centerline HTP surface temperature, providing effective surface temperatures.

$$TW8i2_{eff} = TW8i3 + \frac{\Delta T_{effective}}{2} \tag{4.62}$$

The mean pressure across the region of interest is also evaluated to define a saturation temperature and for plotting the results.

$$h_{8iX}{}^{*} = \frac{\dot{Q}"_{latent}}{T_{sat}(PT801_{mean}) - TW8i2_{eff}} \tag{4.63}$$

The alternate heat flux and heat transfer coefficients are presented as a function of mean pressure in section 5.7.

4.2.9 Evaluating Known Uncertainties

Before drawing conclusions from the test results, evaluation of the uncertainties in the published results is necessary. Since the objective of this investigation is to evaluate condensation heat fluxes and heat transfer coefficients, the uncertainty evaluation will be focused on those calculations. The error associated with those evaluations is the combination of various contributing sources of error.

If values are added or subtracted:

$$a = b + c - d \tag{4.64}$$

Then:

$$\epsilon_a = \pm\sqrt{\epsilon_b{}^2 + \epsilon_c{}^2 + \epsilon_d{}^2} \tag{4.65}$$

If values are multiplied or divided:

$$a = \frac{b \cdot c}{d} \tag{4.66}$$

Then the error is propagated in terms of relative error:

$$\epsilon_a = \pm|a| \cdot \sqrt{\left(\frac{\epsilon_b}{b}\right)^2 + \left(\frac{\epsilon_c}{c}\right)^2 + \left(\frac{\epsilon_d}{d}\right)^2} \tag{4.67}$$

4.2.9.1 Relevant Instrument Uncertainties

The instrument uncertainties necessary for evaluating the heat flux and heat transfer coefficient uncertainties are presented in Table 4-5.

Table 4-5: Relevant Instrument Uncertainties

Measurement Type	**Tag Number**	**Listed Uncertainty**
Thermocouples	TW-xxx, TF-xxx, TH-xxx	3.2°C
Pressure Meter	PT-801	1.4 psi
Level Meter	LDP-801	0.772 inches H_2O
Plate width (between TCs)	--	0.083 inches

4.2.9.2 Uncertainty Based on Measured HTP Surface Temperatures

In determining the heat flux using the HTP thermocouple measurements, the contributing sources of error include the thermocouple measurement uncertainty and the spatial uncertainty of the thermocouple measurements. The value used for thermal conductivity is an assumption and does not have a quantified uncertainty associated with it.

While the evaluation for heat flux is:

$$\dot{Q}"_{8iX} = k_{HTP} \cdot \frac{(TW8i2 - TW8i4)}{Th_{HTP}} \tag{4.68}$$

The error evaluation for heat flux is:

$$\epsilon_{\dot{Q}"} = \pm\, \dot{Q}"_{8iX} \cdot \sqrt{\left(\frac{\sqrt{2 \cdot {\epsilon_T}^2}}{TW8i2 - TW8i4}\right)^2 + \left(\frac{\epsilon_{Th}}{Th_{HTP}}\right)^2} \tag{4.69}$$

Determining the heat transfer coefficient using the HTP measurements also requires evaluating the bulk steam temperature. The bulk steam temperature is assumed to be the saturated temperature at the measured total pressure; there are no quantified uncertainties associated with this assumption.

The evaluation for heat transfer coefficient is:

$$h_{8iX} = \frac{\dot{Q}"_{8iX}}{[T_{sat}(PT801) - TW8i2]} \tag{4.70}$$

The heat flux and associated error were previously evaluated. It is useful to evaluate the error associated with the saturation temperature separately.

$$\epsilon_{Tsat} = \pm\, \frac{T_{sat}(PT801 + |\epsilon_P|) - T_{sat}(PT801 - |\epsilon_P|)}{2} \tag{4.71}$$

The error evaluation for heat transfer coefficient is:

$$\epsilon_h = \pm\, h_{8iX} \cdot \sqrt{\left(\frac{\epsilon_{\dot{Q}"}}{\dot{Q}"_{8iX}}\right)^2 + \left(\frac{\sqrt{{\epsilon_{Tsat}}^2 + {\epsilon_T}^2}}{T_{sat}(PT801) - TW8i2}\right)^2} \tag{4.72}$$

4.2.9.3 Uncertainty Based on Corrected Surface Temperatures

Evaluating the error associated with the surface temperature corrections require extensive calculations.

a) The first step is to evaluate the error in the calculated condensate density. The calculated density is a function of temperature and pressure.

$$\rho_{liq} = \rho(PT801, TF804) \tag{4.73}$$

$$\epsilon_{\rho} = \pm \sqrt{\left(\frac{\rho(PT801 + |\epsilon_P|, TF804) - \rho(PT801 - |\epsilon_P|, TF804)}{2}\right)^2 \ldots + \left(\frac{\rho(PT801, TF804 + |\epsilon_T|) - (PT801, TF804 - |\epsilon_T|)}{2}\right)^2} \tag{4.74}$$

b) Density and the liquid level measurement are used to calculate instantaneous liquid mass.

$$m_{liq} = \rho_{liq} \cdot LDP801 \cdot A_{HPC} \tag{4.75}$$

$$\epsilon_{mliq} = \pm\, m_{liq} \cdot \sqrt{\left(\frac{\epsilon_{LDP}}{LDP801}\right)^2 + \left(\frac{\epsilon_{\rho}}{\rho(PT801, TF804)}\right)^2} \tag{4.76}$$

c) The specific heat of vaporization is based on the saturated pressure.

$$h_{fg} = h_{sat,v}(PT801) - h_{sat,l}(PT801) \tag{4.77}$$

$$\epsilon_{hfg} = \pm \frac{1}{2} \cdot \Big[\big[h_{sat,v}(PT801 + |\epsilon_P|) - h_{sat,l}(PT801 + |\epsilon_P|)\big] - \big[h_{sat,v}(PT801 - |\epsilon_P|) - h_{sat,l}(PT801 - |\epsilon_P|)\big]\Big] \tag{4.78}$$

d) The latent heat released is associated with the instantaneous liquid mass and specific latent heat.

$$E_{latent} = m_{liq} \cdot (h_{sat,v}(PT801) - h_{sat,l}(PT801)) \tag{4.57}$$

$$\epsilon_{latent} = \pm\, E_{latent} \cdot \sqrt{\left(\frac{\epsilon_{mliq}}{m_{liq}}\right)^2 + \left(\frac{\epsilon_{hfg}}{h_{sat,v}(PT801) - h_{sat,l}(PT801)}\right)^2} \tag{4.79}$$

e) The rate of change of latent heat is the difference between the initial and final instantaneous latent heat divided by the region of interest (RB-LB).

$$\Delta\dot{E}_{latent} = \frac{E_{latent}(RB) - E_{latent}(LB)}{RB - LB} \tag{4.58}$$

$$\epsilon_{\dot{\Delta}latent} = \pm\frac{\sqrt{2\cdot(\epsilon_{latent})^2}}{RB - LB} \tag{4.80}$$

f) The unsubmerged area of the heat transfer plate is evaluated with the liquid level measurement.

$$A_{HTP,unsub} = (H_{HTP} - LDP801(LB{:}RB))\cdot W_{HTP} \tag{4.59}$$

$$\epsilon_{Ahtp} = \pm\,\epsilon_{LDP}\cdot W_{HTP} \tag{4.81}$$

g) The heat flux on the plate is calculated with latent heat rate and available surface area.

$$\dot{Q}"_{latent} = \frac{\Delta\dot{E}_{latent}}{\mathbf{mean}[A_{HPT,unsub}]} \tag{4.60}$$

$$\epsilon_{Q"latent} = \pm\,\dot{Q}"_{latent}\cdot\sqrt{\left(\frac{\epsilon_{\dot{\Delta}latent}}{\Delta\dot{E}_{latent}}\right)^2 + \left(\frac{\epsilon_{Ahtp}}{\mathbf{mean}[A_{HPT,unsub}]}\right)^2} \tag{4.82}$$

h) The effective temperature difference across the plate required to produce that heat flux is evaluated.

$$\Delta T_{effective} = \frac{\dot{Q}"_{latent}\cdot Th_{HTP}}{k_{HTP}} \tag{4.61}$$

$$\epsilon_{\Delta Teff} = \pm\,\Delta T_{effective}\cdot\left(\frac{\epsilon_{Q"latent}}{\dot{Q}"_{latent}}\right) \tag{4.83}$$

i) The effective containment side surface temperature is evaluated using the effective temperature difference and the midline HTP temperature (TW8X3).

$$TW8i2_{eff} = TW8i3 + \frac{\Delta T_{effective}}{2} \tag{4.62}$$

$$\epsilon_{TW8i2*} = \pm\sqrt{\epsilon_T{}^2 + \left(\frac{\epsilon_{\Delta Teff}}{2}\right)^2} \tag{4.84}$$

j) The effective heat transfer coefficient is evaluated with the effective heat flux and effect surface temperature.

$$h_{8iX}{}^* = \frac{\dot{Q}"_{latent}}{T_{sat}(PT801_{mean}) - TW8i2_{eff}} \tag{4.63}$$

$$\epsilon_{h*} = \pm h_{8iX}{}^* \cdot \sqrt{\left(\frac{\epsilon_{Q"latent}}{\dot{Q}"_{latent}}\right)^2 + \left(\frac{\sqrt{\epsilon_{Tsat}{}^2 + \epsilon_{TW8i2*}{}^2}}{T_{sat}(PT801_{mean}) - TW8i2_{eff}}\right)^2} \tag{4.85}$$

5 Results

5.1 Quick Look

Before jumping into the analysis of each test, this section briefly describes how each test proceeded. The HPC pressures are shown over the course of each test with markings for the regions of interest within which the detailed analysis will be focused.

The first set of tests saw pressure rise in the containment until either the pressure approached operating limits or a predetermined amount of time had elapsed. The cases with the lower steam flow (Test 1.1, Test 1.3, and Test 1.5) pressurized rather slowly as the condensation rate followed closely behind the rate of steam addition to the containment. Each of these tests was terminated after 90 minutes of testing had elapsed while the containment pressure remained well below design limits. The cases which used a higher power and steam flow (Test 1.2, Test 1.4, and Test 1.6) pressurized relatively rapidly as the condensation rate was outpaced by the rate of steam addition. These high power tests were terminated between 18 and 35 minutes once the containment design pressure was reached.

Table 5-1: Description of the first set of tests

	Applied Power	Steam Flow Rate	Initial Pressure	Final Pressure	Final NCG Fraction	Duration
Test 1.1	40 kW	~0.0133 kg/s	0.07 bar	8.73 bar	0.017	90 min
Test 1.2	80 kW	~0.0264 kg/s	0.07 bar	20.59 bar	0.007	34 min
Test 1.3	40 kW	~0.0133 kg/s	.52 bar	10.94 bar	0.096	90 min
Test 1.4	80 kW	~0.0264 kg/s	.52 bar	20.59 bar	0.052	24 min
Test 1.5	40 kW	~0.0133 kg/s	1.31 bar	14.42 bar	0.186	90 min
Test 1.6	80 kW	~0.0264 kg/s	1.32 bar	20.60 bar	0.124	18 min

Figure 5-1 and Figure 5-2 show the containment pressures through the duration of each test with markings for the left and right bounds of the regions of interest. The low steam flow rates lead to a relatively unsteady pressurization in the containment, as can be seen in Figure 5-1. This appears to be due to the pressure regulating valve working to hold such a low flow rate at choked conditions (large pressure drop from secondary to containment). A region of interest of 4000 seconds was selected for the low flow rate tests to avoid the more transient moments of the tests. A shorter region of 500 seconds was selected for the rapidly evolving high flow rate tests.

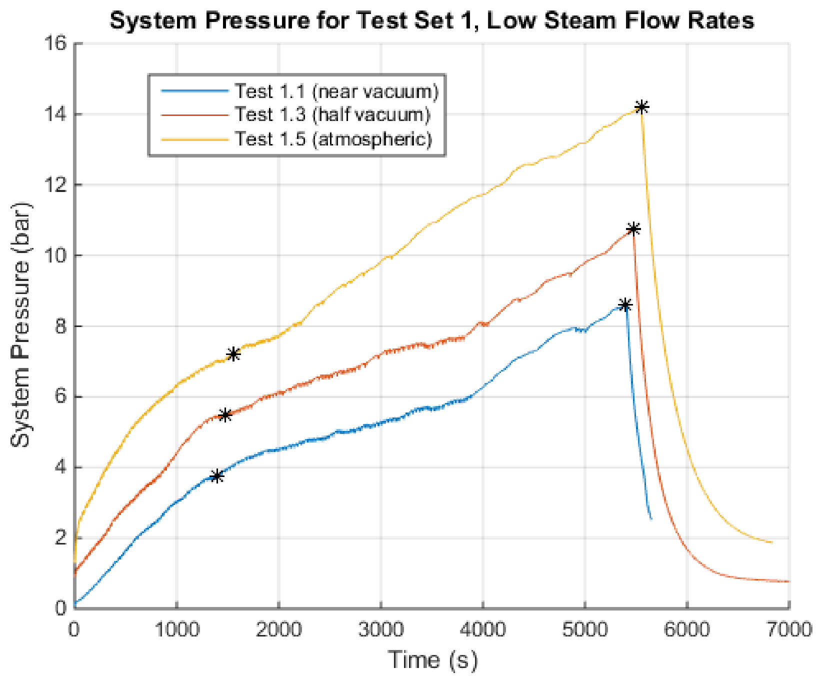

Figure 5-1: HPC pressure for Test Set 1 (low flow rates)

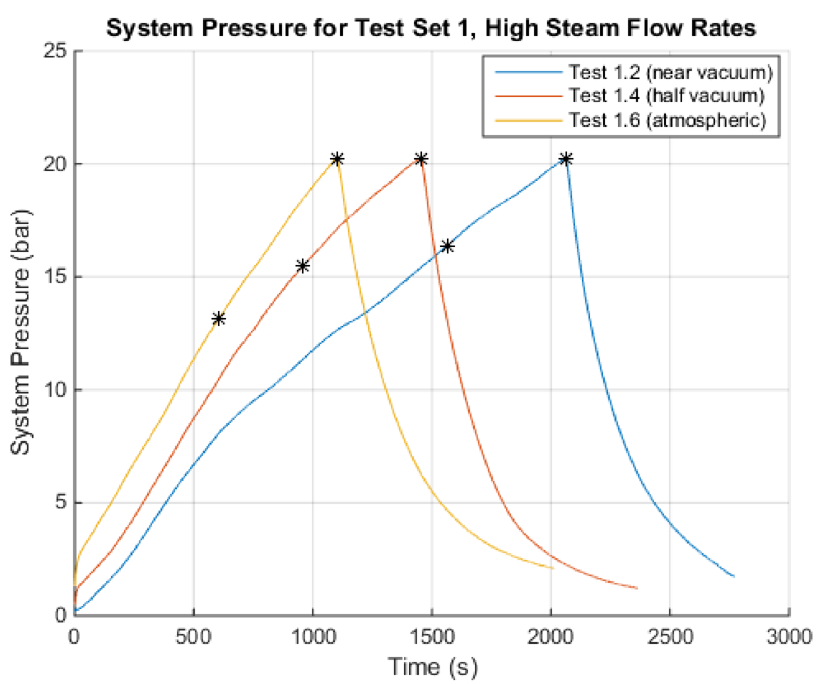

Figure 5-2: HPC pressure for Test Set 1 (high flow rates)

The temperature of the cooling pool was inconsistent between the first set of tests. The low steam flow rate tests lasted far longer than the high flow rate tests, and as a result significantly more energy was imparted into the system. Additionally, the initial temperature of the pool varied between tests. Tests 1.1 and 1.5 were conducted with initial average CPV temperatures of 26°C and 19°C respectively while the average of the other four tests was about 9°C. The inconsistent pool temperatures significantly impacted the heat fluxes but the heat transfer coefficients should not be affected.

The second round of tests aimed to improve testing conditions and provide a second data set for the analysis of containment condensation. An attempt was made to isolate the pressure effect from the transient influence of continuously increasing pressures and temperatures by performing a series of quasi steady state tests. Each was devised to reach and maintain a unique pressure.

Table 5-2: Quasi steady pressures reached in the second set of tests

	Average NCG Fraction	*Pressure Plateau*
Test 2.1	0.025	4-6 bar
Test 2.2	0.017	7-9 bar
Test 2.3	0.012	11-13 bar
Test 2.4	0.009	15-17 bar
Test 2.5	0.278	7-9 bar
Test 2.6	0.203	11-13 bar
Test 2.7	0.156	15-17 bar

While containment pressure was not maintained exceptionally steady during each quasi-steady period, the result, as shown in Figure 5-3 and Figure 5-4, was satisfactory. In fact, the aim and expectation for each test was to see the HPC pressure initially decrease following the transition to the reduced steam flow before gradually increasing again. The pressure is difficult to keep constant because the heat transfer rates inherently change as the condensate submerges the HTP and the heat sink temperatures increases. Figure 5-3 and Figure 5-4 below show the containment pressure for the quasi-steady tests performed with the near-vacuum and atmospheric initial conditions in the containment.

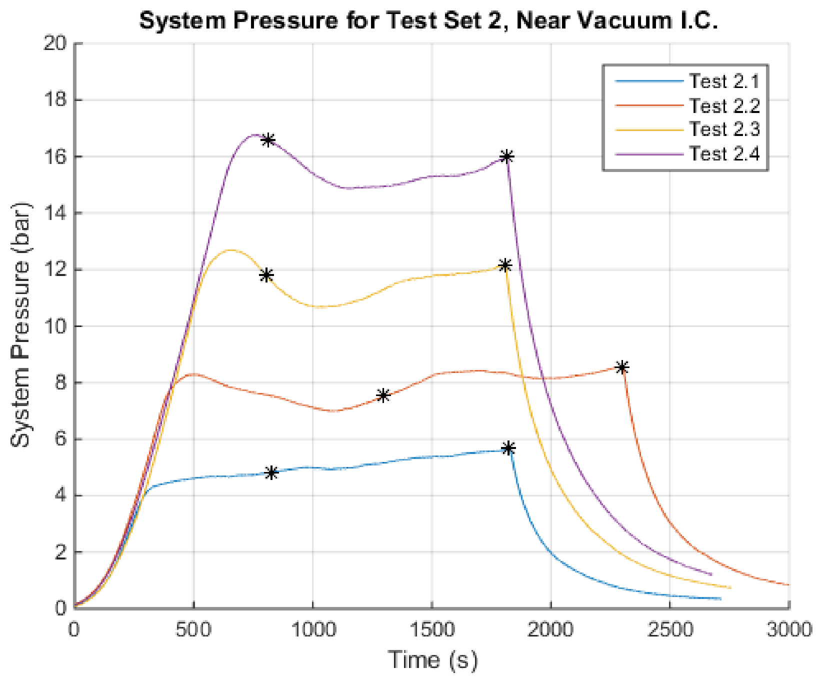

Figure 5-3: HPC pressure for Test Set 2 (near vacuum I.C.)

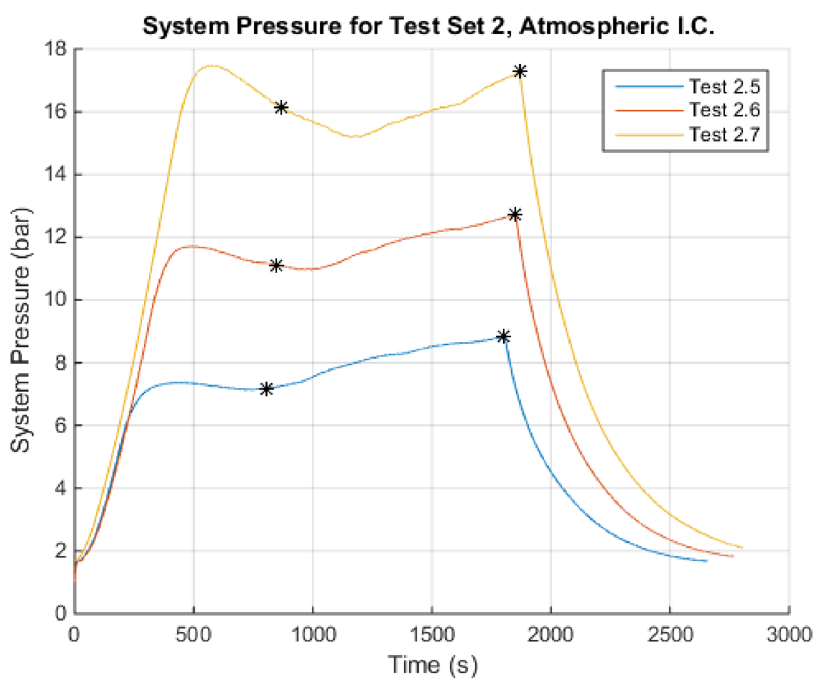

Figure 5-4: HPC pressure for Test Set 2 (atmospheric I.C.)

This second round of testing was performed with more consistency in initial and boundary conditions, facilitating comparisons between tests. One important improvement was that the tests were shorter and each lasted the same amount of time (with exception of Test 2.2), reducing the differences in heat sink temperature between each test.

5.2 Regions of Interest

The regions of interest for each test are selected to isolate the more steady periods of each test. The transient effects were most significant during the initial moments of the transients as the structures were rapidly heating up. The total duration of the region of interest was kept consistent between the tests and each ends just prior to the termination of steam supply. The left and right bounds for each region are presented in Table 5-3. The ranges of the plots shown in the previous section were modified from the original data set and should not be compared to the bounds list below.

Table 5-3: Left and right bounds of the regions of interest selected for detailed analysis

Test	**Left Bound**	**Right Bound**	**Duration (s)**
Test Set 1			
Test 1.1	3951	7951	4000
Test 1.2	1641	2141	500
Test 1.3	4460	6460	4000
Test 1.4	1595	2095	500
Test 1.5	4918	8918	4000
Test 1.6	1793	2293	500
Test Set 2			
Test 2.1	1523	2523	1000
Test 2.2	3167	4167	1000
Test 2.3	880	1880	1000
Test 2.4	1372	2372	1000
Test 2.5	3842	4842	1000
Test 2.6	1325	2325	1000
Test 2.7	997	1997	1000

5.3 Mass Balance

The mass balance consists of comparing the cumulative steam flow into the containment with the instantaneous vapor and liquid mass measured in the HPC. Section 4.2.5 describes of the calculations involved.

In lieu of displaying the results for all 13 tests, the mass comparison is presented graphically for Test 1.1, Test 1.6, Test 2.1, and Test 2.7 to represent the limits of the test conditions. Test 1.1 was performed with a low steam flow rate and a near-vacuum initial HPC pressure, while Test 1.6 was performed with a high steam flow rate and atmospheric HPC initial pressure. Test 2.1 was conducted with a near vacuum HPC and achieved a pressure plateau of roughly 5 bar, while Test 2.7 was performed with an atmospheric HPC and reached a pressure plateau of about 16 bar.

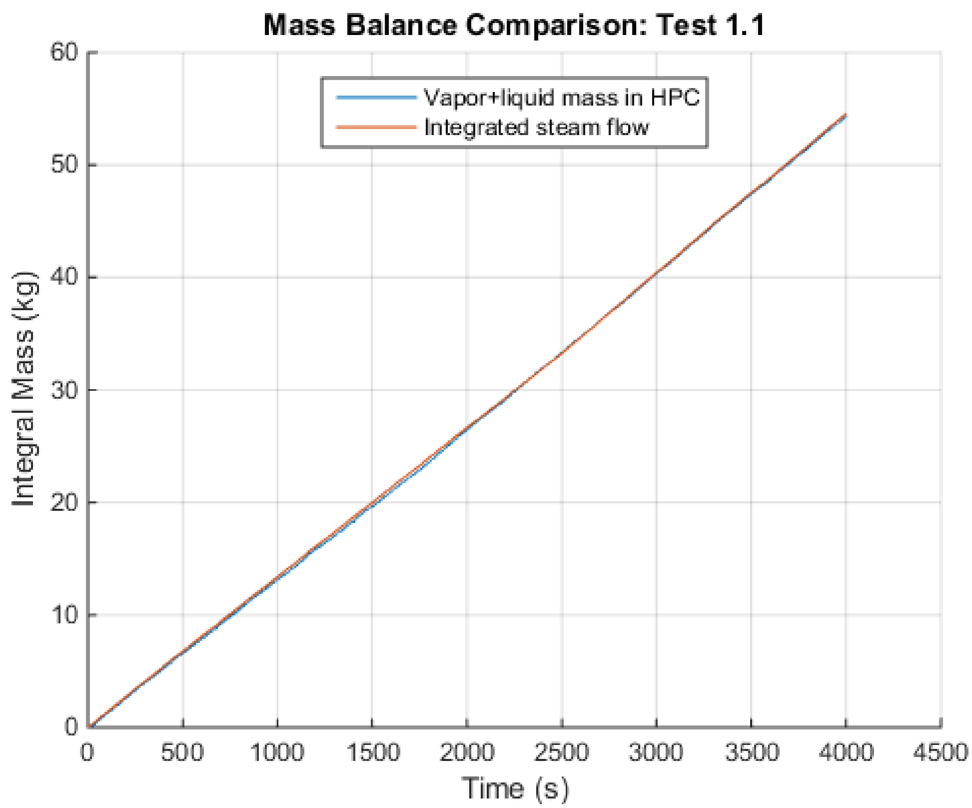

Figure 5-5: HPC mass balance, Test 1.1

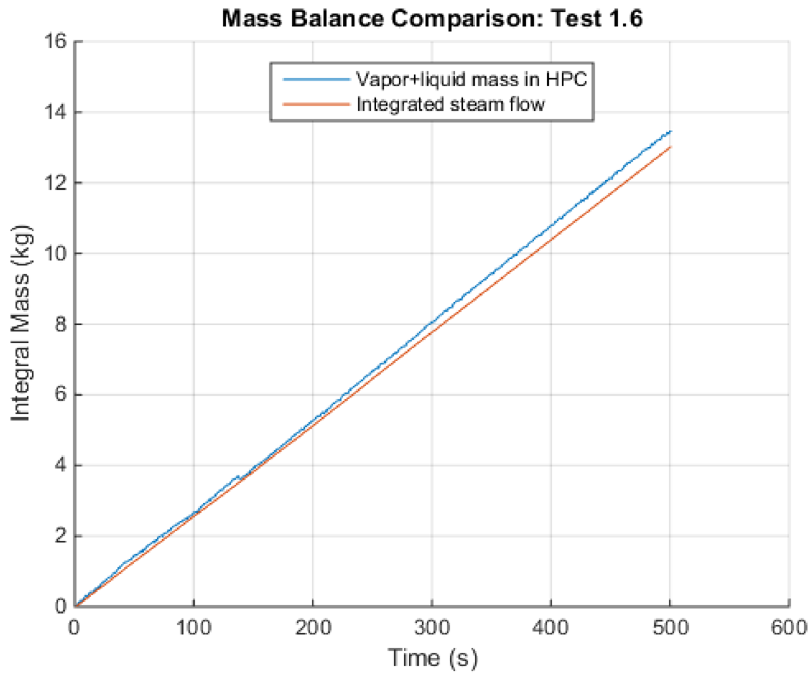

Figure 5-6: HPC mass balance, Test 1.6

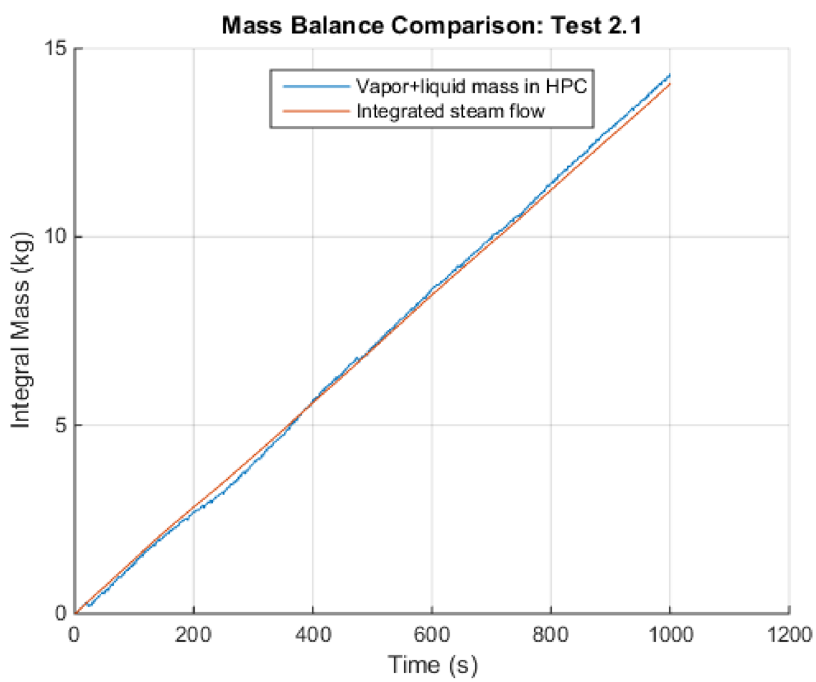

Figure 5-7: HPC mass balance, Test 2.1

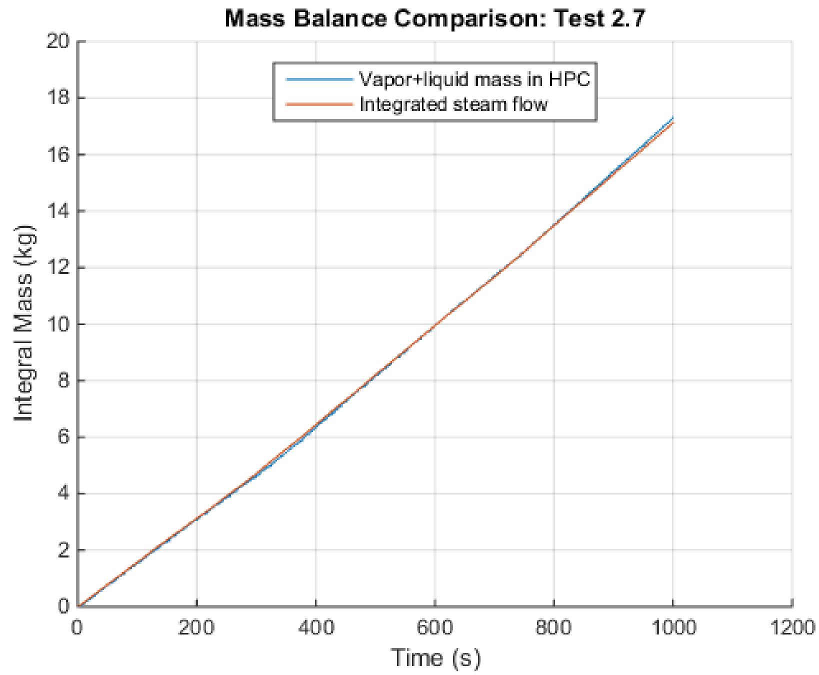

Figure 5-8: HPC mass balance, Test 2.7

Figure 5-9: Integral mass error for Test Set 1 (low flow rates)

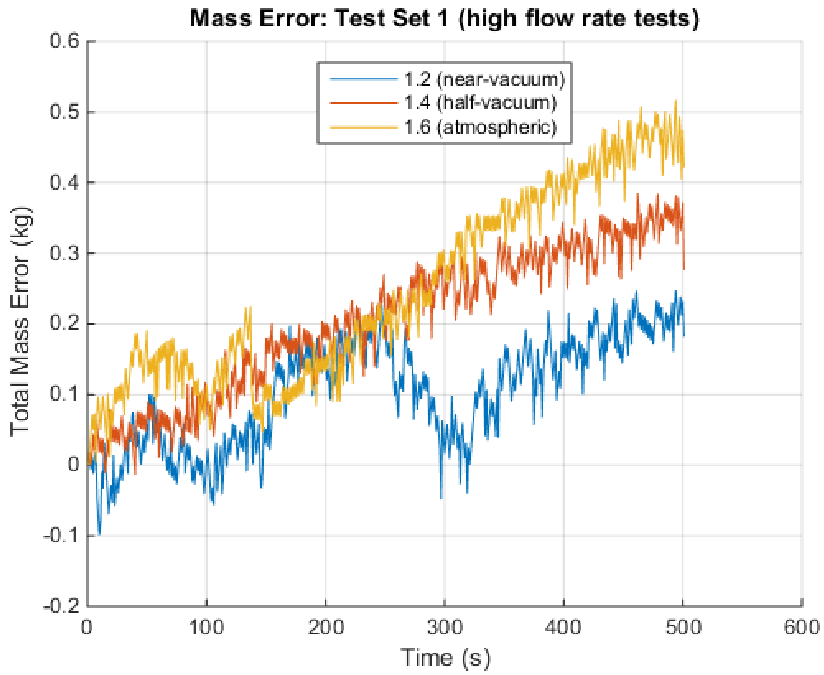

Figure 5-10: Integral mass error for Test Set 1 (high flow rates)

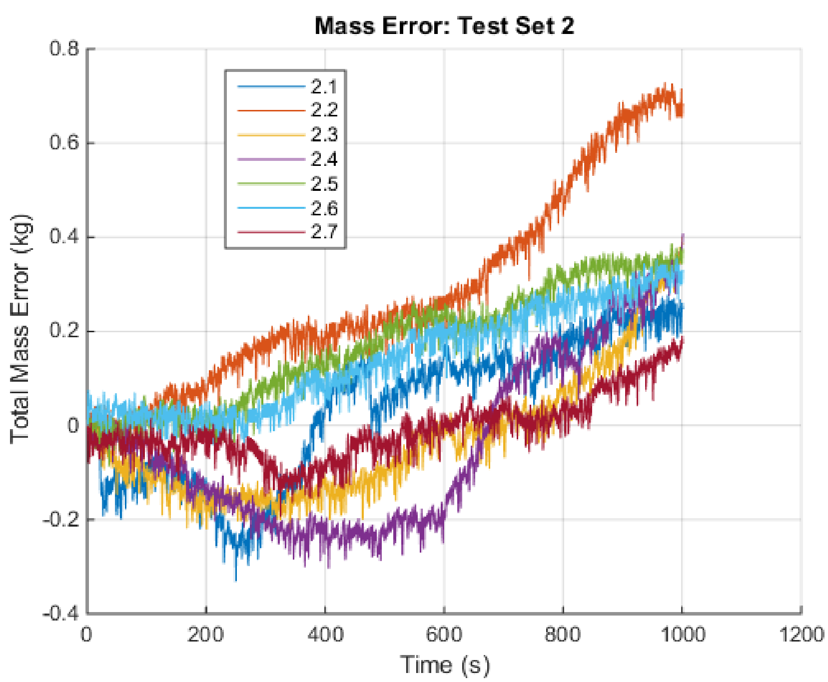

Figure 5-11: Integral mass error for Test Set 2

Table 5-4: Mass error and error percent

Test	Mass Error (kg)	Mass Error Percent
Test Set 1		
Test 1.1	-0.2249	-0.41 %
Test 1.2	0.1817	1.37 %
Test 1.3	0.7228	1.32 %
Test 1.4	0.2762	2.10 %
Test 1.5	-0.9633	-1.82%
Test 1.6	0.4210	3.23 %
Test Set 2		
Test 2.1	0.2476	1.76%
Test 2.2	0.6843	4.26%
Test 2.3	0.3831	2.05%
Test 2.4	0.4077	1.96%
Test 2.5	0.3755	2.99%
Test 2.6	0.3313	2.18%
Test 2.7	0.1731	1.01%

In general, the mass balance comparison shows good agreement between the mass measurement methods. It should be noted that the error values presented in Table 5-4 are subject to changing significantly when different bounds are selected for the region of interest. Attention was taken not to manipulate the region of interest to suggest a favorable mass balance.

5.4 Energy Balance

There are several measured energy flows to consider in these condensation tests. The internal energy of the vapor, condensate, noncondensable gas, HTP, and CPV are compared to the energy carried into the system from the steam supply. Most importantly, the HTP conduction calculations are compared to the heat removed from the HPC and the increase in internal energy of the CPV. Section 4.2.6 describes the calculations involved. A representative comparison is detailed for Test 1.1, Test 1.6, Test 2.1, and Test 2.7 while the energy errors are presented for all of the tests.

The calculations for the heat removed from the HPC (sensible heat, phase change) relative to the steam inlet flow enthalpy were shown to have approximately the same error as the mass calculations, a logical result of similar calculations. The energy balance shown in Figure 5-12 through Figure 5-15 is a comparison of the change in internal energy of the pool, the HPC heat removed, and the integration of the conductive heat flux through the plate. The heat removed from the HPC should be considered the baseline for comparing the other two energy flows.

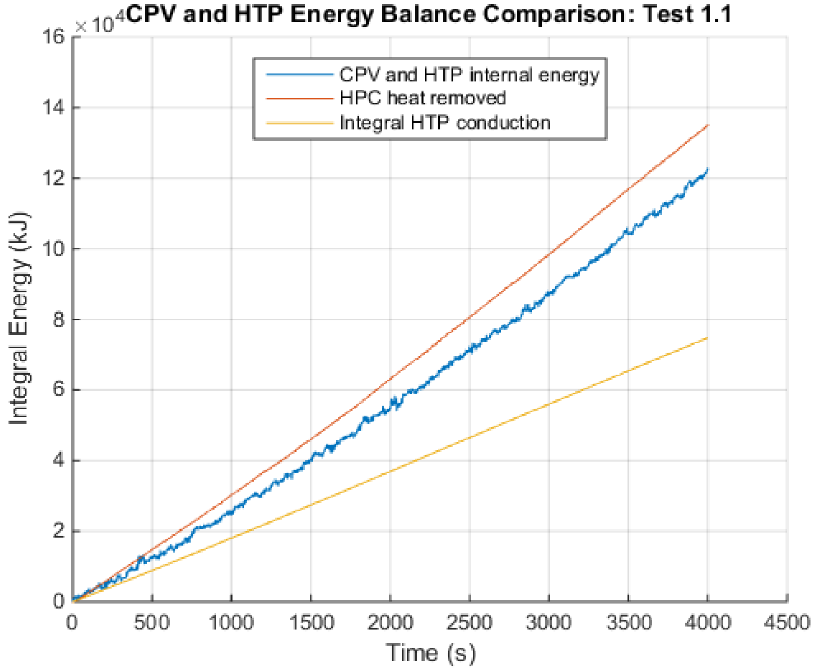

Figure 5-12: Energy balance across HTP, Test 1.1

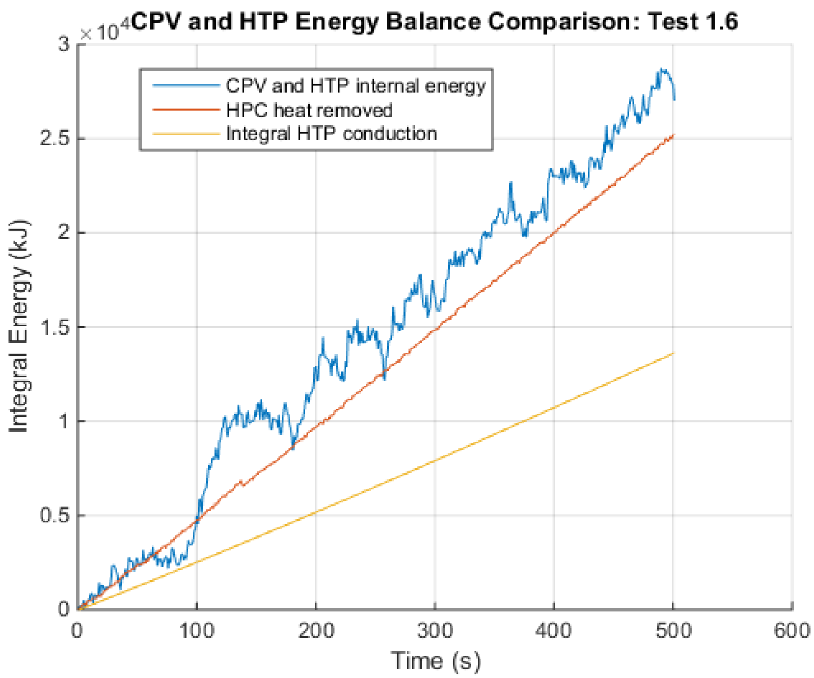

Figure 5-13: Energy balance across HTP, Test 1.6

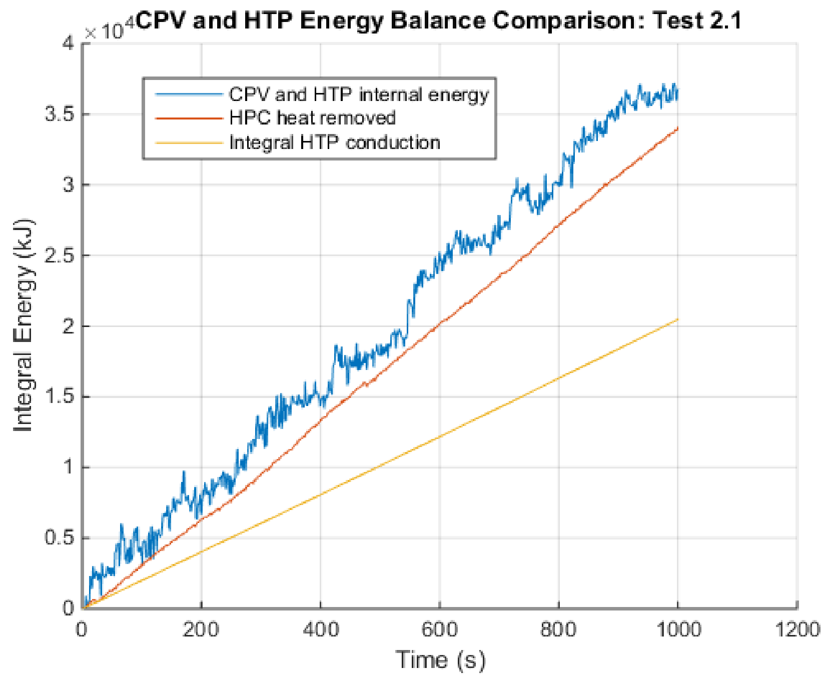

Figure 5-14: Energy balance across HTP, Test 2.1

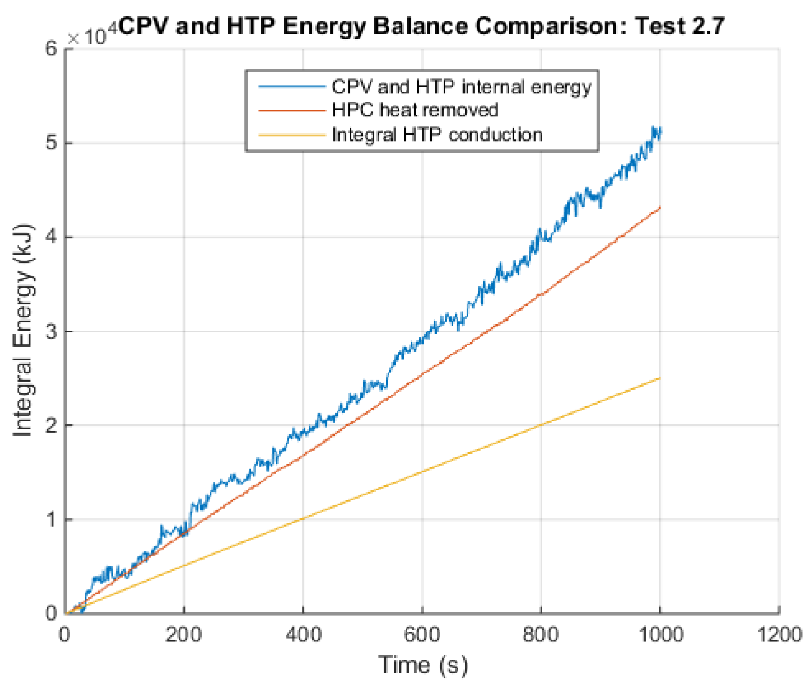

Figure 5-15: Energy balance across HTP, Test 2.7

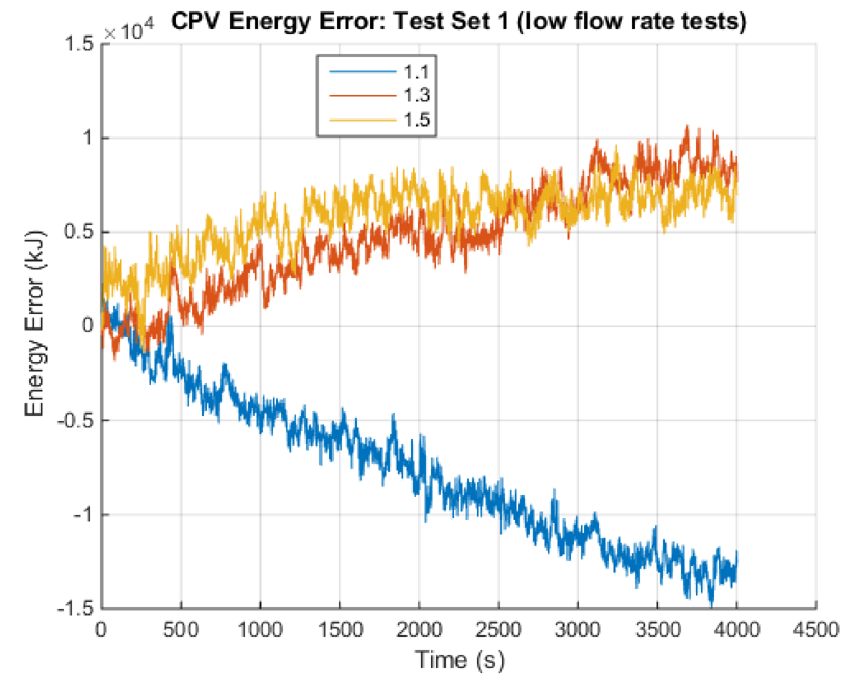

Figure 5-16: Integral CPV energy error for Test Set 1 (low flow rates)

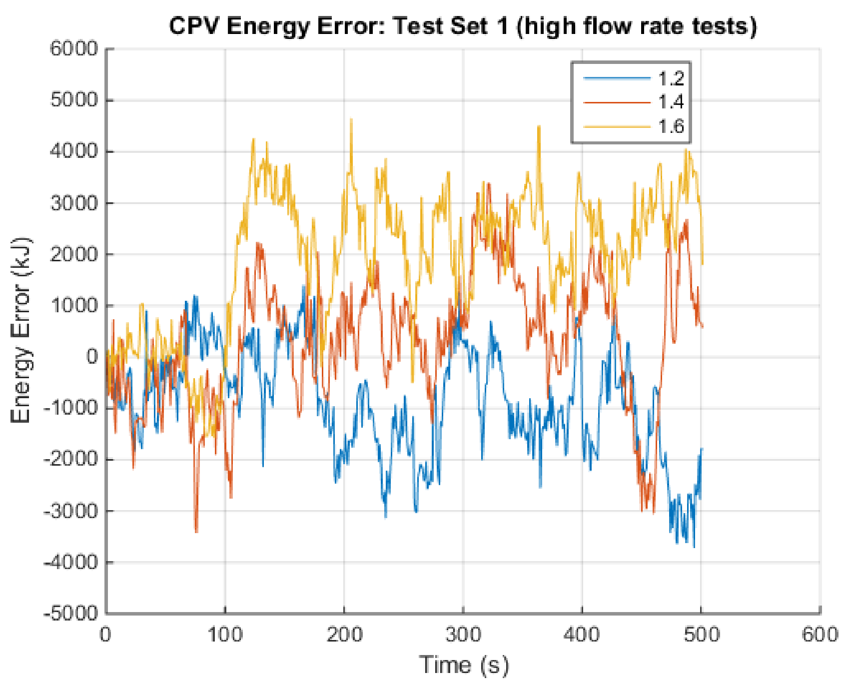

Figure 5-17: Integral CPV energy error for Test Set 1 (high flow rates)

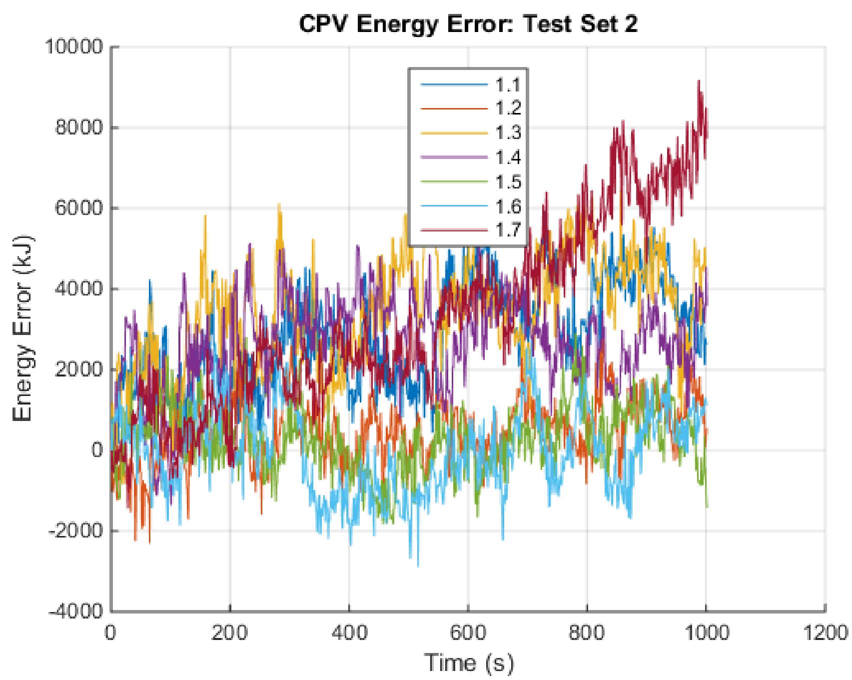

Figure 5-18: Integral CPV energy error for Test Set 2

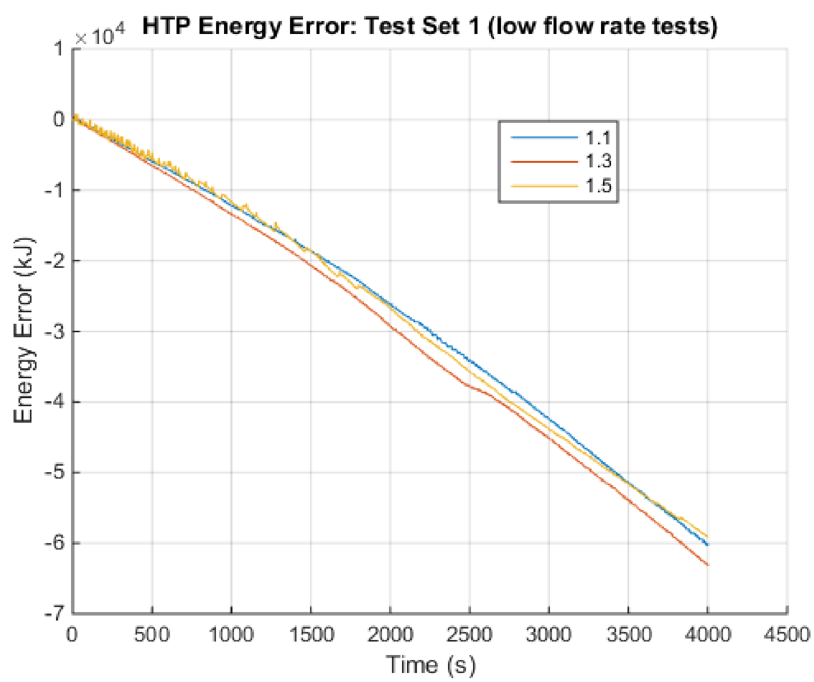

Figure 5-19: Integral HTP energy error for Test Set 1 (low flow rates)

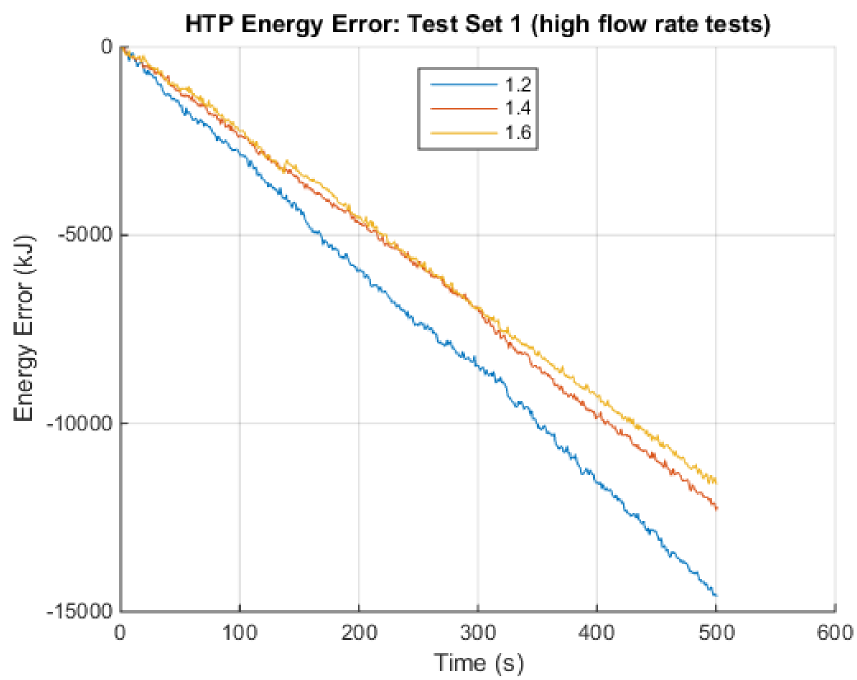

Figure 5-20: Integral HTP energy error for Test Set 1 (high flow rates)

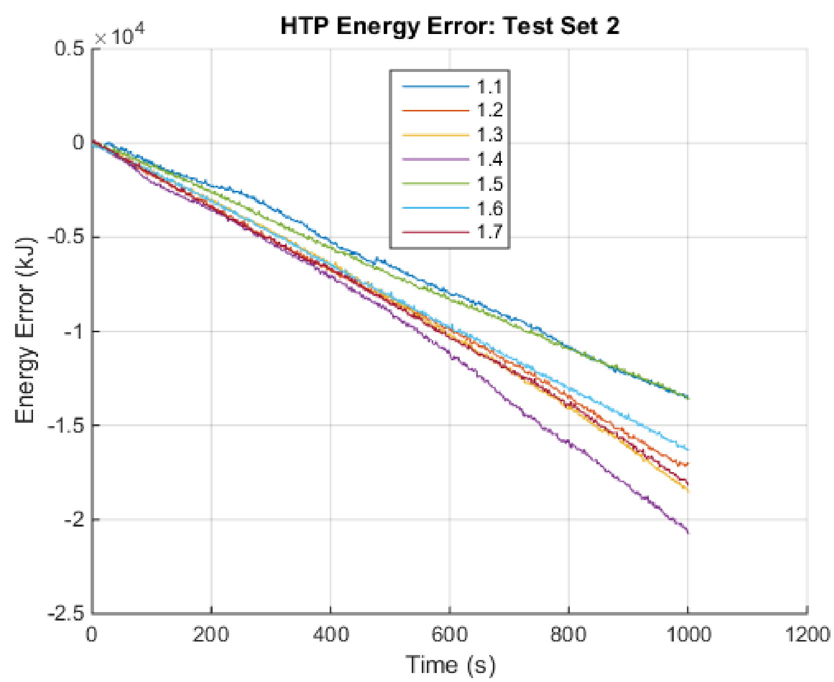

Figure 5-21: Integral HTP energy error for Test Set 2

Table 5-5: Energy errors and percent errors

Test	HPC error (kJ)	HPC error %	CPV error (kJ)	CPV error %	HTP error (kJ)	HTP error %	System error (kJ)	System error %
Set 1								
Test 1.1	-407.6	-0.26	-12332.0	-9.12	-60719.0	-44.9	-12740.0	-8.17
Test 1.2	616.3	1.62	-1808.0	-5.98	-14574.0	-48.2	-708.0	-0.94
Test 1.3	882.3	0.57	7663.0	5.43	-64529.0	-45.7	8545.0	5.49
Test 1.4	916.7	2.43	564.0	2.07	-12205.0	-44.9	1727.0	2.27
Test 1.5	-2213.8	-1.48	6964.0	5.21	-61062.0	-45.7	4750.0	3.17
Test 1.6	1469.8	3.95	1790.0	7.10	-11601.0	-46.0	1813.0	2.44
Set 2								
Test 2.1	231.0	0.56	2623.9	7.70	-13644.0	-40.0	2854.9	6.97
Test 2.2	1608.9	3.46	550.7	1.36	-17125.0	-42.2	2159.6	4.65
Test 2.3	418.2	0.76	4342.5	9.66	-18672.0	-41.5	4760.7	8.85
Test 2.4	481.4	0.81	3579.2	7.16	-20953.0	-41.9	4060.6	6.81
Test 2.5	616.6	1.70	-1423.3	-4.40	-14103.0	-42.6	-806.7	-2.23
Test 2.6	478.0	1.10	1112.3	2.88	-16800.0	-43.5	1590.3	3.64
Test 2.7	224.3	0.46	7723.2	17.85	-18475.0	-42.7	7947.5	16.2

The energy balance across the HTP suggests reasonable validity of the internal energy calculations for the CPV. Recall this calculation involved an extrapolation of upper CPV temperatures to evaluate an average pool temperature (Assumption 6). The error in this measurement was greater over long testing durations. The shape of the axial temperature profiles measured in the upper CPV is observed to change along the duration of the tests, perhaps due to natural circulation timescales. It is accepted that the linear extrapolation for CPV temperatures cannot accurate account for this. This method appears to be more likely to over predict the change in internal energy when compared to the heat removed from the HPC. While the confidence in the CPV measurement is admittedly low, the over predication of internal energy change suggests that most of the heat being removed from the HPC is likely going into the CPV through the heat transfer plate and the environmental heat losses are small.

Figure 5-19 through Figure 5-21 show that the conductive heat flux measurements for the plate appear to be consistently under predicting the actual heat transfer. This is discussed in detail in Section 5.7, but the primary reason is likely imprecise measurement of HTP surface temperatures with the embedded thermocouples.

5.5 Condensation Rates vs. System Pressure

Although the energy balance showed that the measured conductive heat flux was significantly under predicting actual heat transfer rates, the trends observed with those measurements may still be relevant. The pressure effect should still be evaluated employing this measurement. The average heat flux and heat transfer coefficient is shown for each case. The 81X level thermocouple measurements are not included in the averages. Figure 5-22 through Figure 5-25 present the measured condensation heat fluxes and heat transfer coefficients as a function of system pressure.

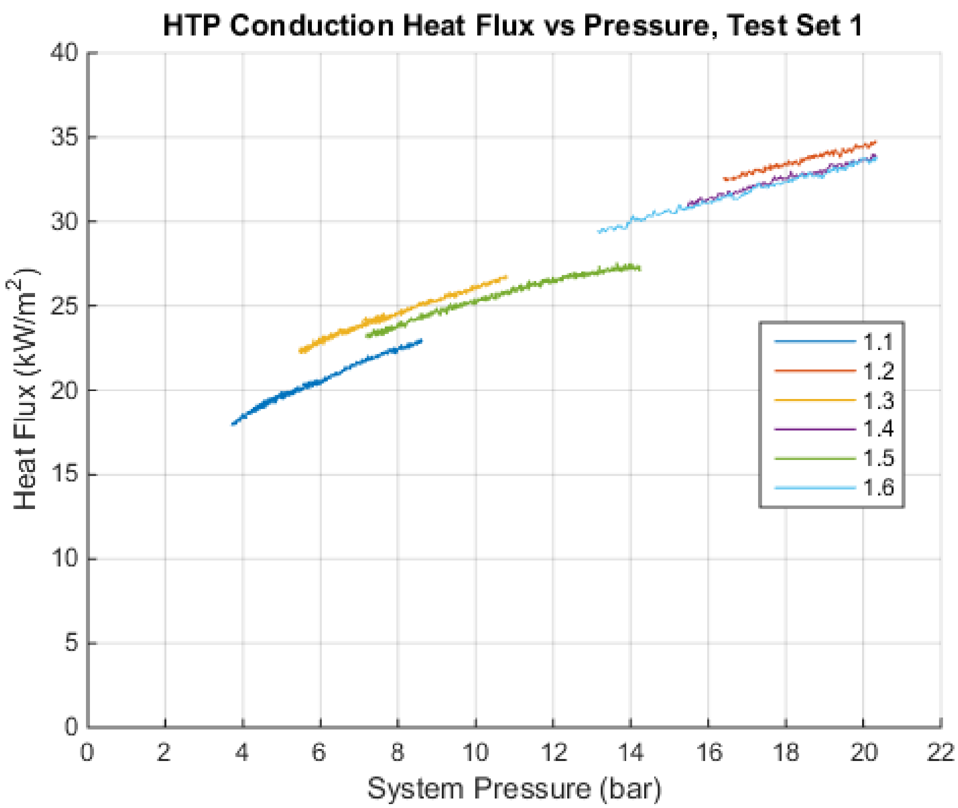

Figure 5-22: Average heat flux from HTP measurements for Test Set 1

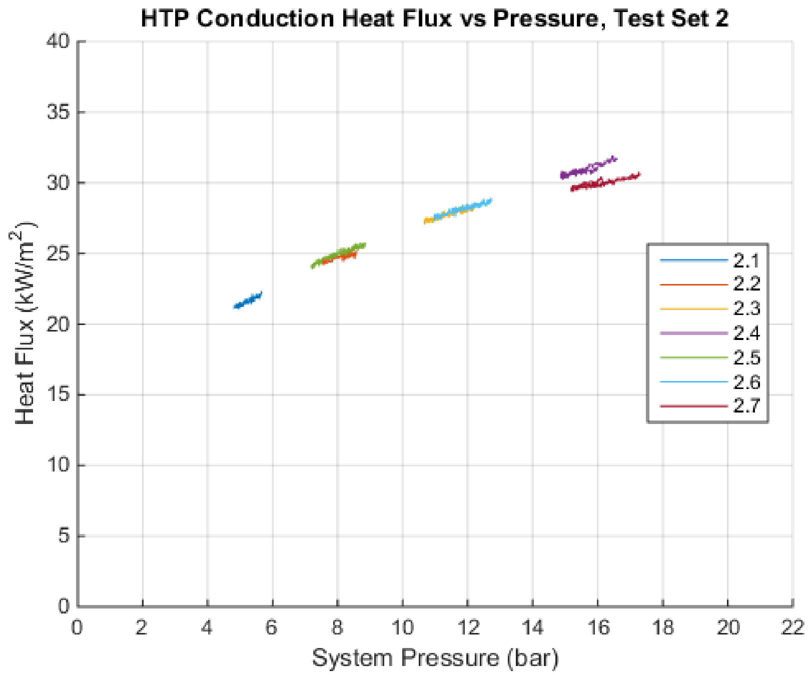

Figure 5-23: Average heat flux from HTP measurements for Test Set 2

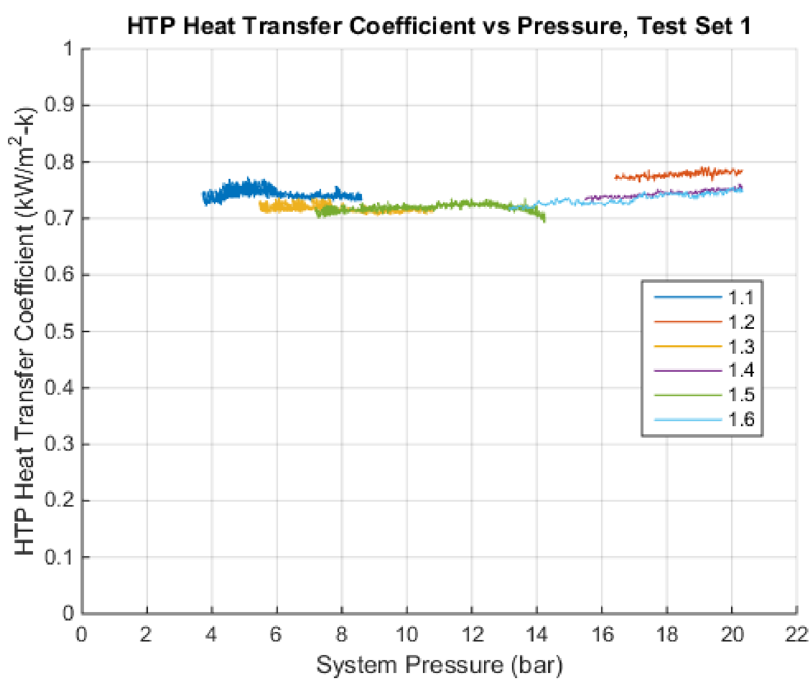

Figure 5-24: Average heat transfer coefficient from HTP measurements for Test Set 1

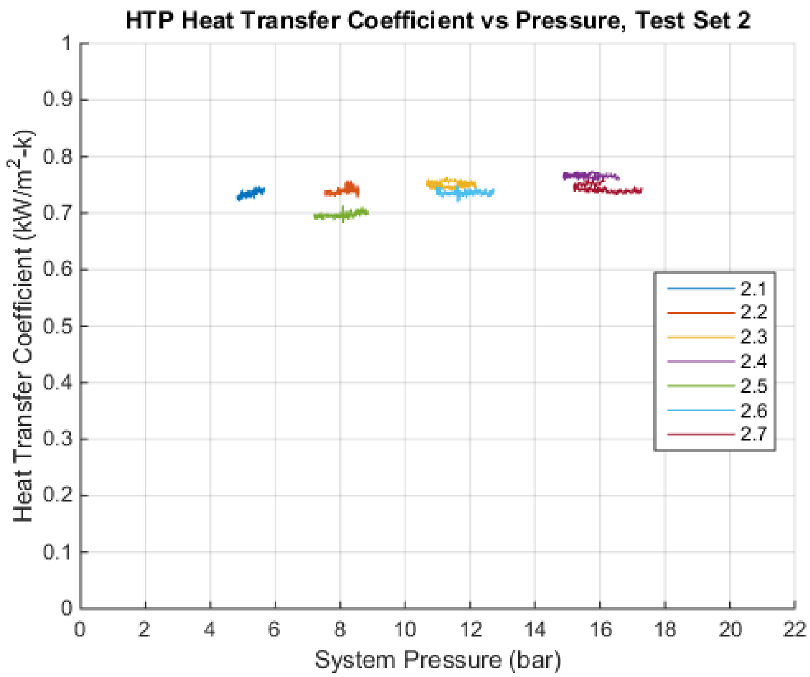

Figure 5-25: Average heat transfer coefficient from HTP measurements for Test Set 2

The condensation heat flux as measured with the HTP thermocouples shows a significant increase with pressure. However, this is appears to be attributable to the increased driving force as saturation temperature increases. These results suggest heat transfer coefficients do not change significantly on system pressure. This result is consistent between both the transient cases and quasi steady tests.

5.6 Condensation Rates vs. Noncondensable Gas Inventory

Figure 5-22 through Figure 5-25 do not show much of a relationship between the initial air inventory and the condensation heat flux measurement. This is because the air seems to settle at the bottom of the containment, where the heat fluxes and heat transfer coefficients are not generally measured. If the partial set of 81X thermocouples is considered, the heat flux reduction at the bottom becomes evident. Figure 5-26 shows the heat flux at all 6 thermocouple elevations for Test 2.2 and Test 2.5. These tests maintained the same quasi steady pressure, however the initial noncondensable inventory is roughly 15 times greater for Test 2.5.

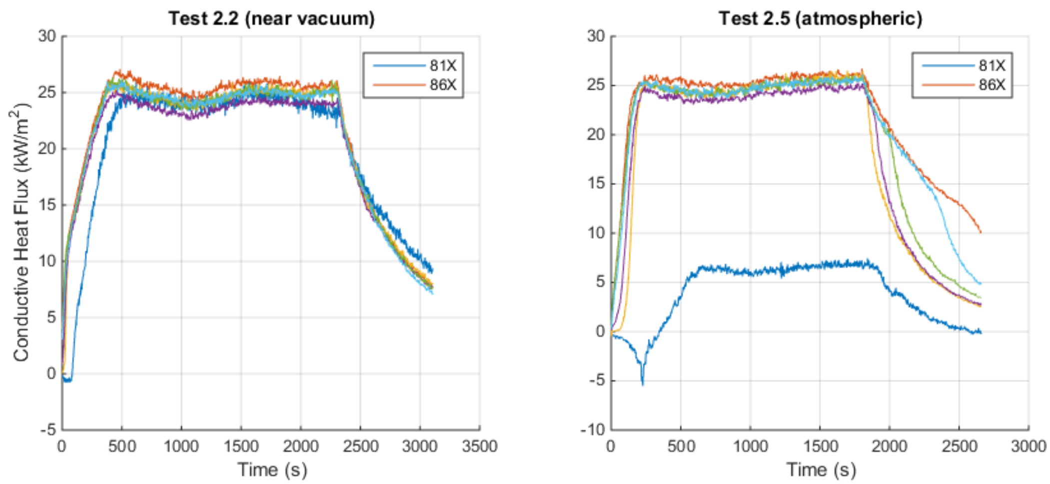

Figure 5-26: Conduction heat flux measured at six axial levels on the HTP

This can also be seen with higher on the HTP when the steam supply is terminated and the remaining steam volume condenses. As the HPC depressurizes, the noncondensable gases expand back up into the containment. A sharp decrease in heat flux climbs the height of the HTP, accompanying the expansion of the gasses. Figure 5-27 compares this effect for 3 different noncondensable inventories.

Thermocouples on the insulated wall of the HPC (TW892, TW893, TW894) provide a representative measurement of bulk steam temperatures. Regardless of noncondensable inventory, these thermocouples consistently measured saturation temperatures at the overall system pressure. This implies the upper region of the containment was relatively free of noncondensable gas as the partial pressure of vapor in the upper regions of the containment was always near the system pressure.

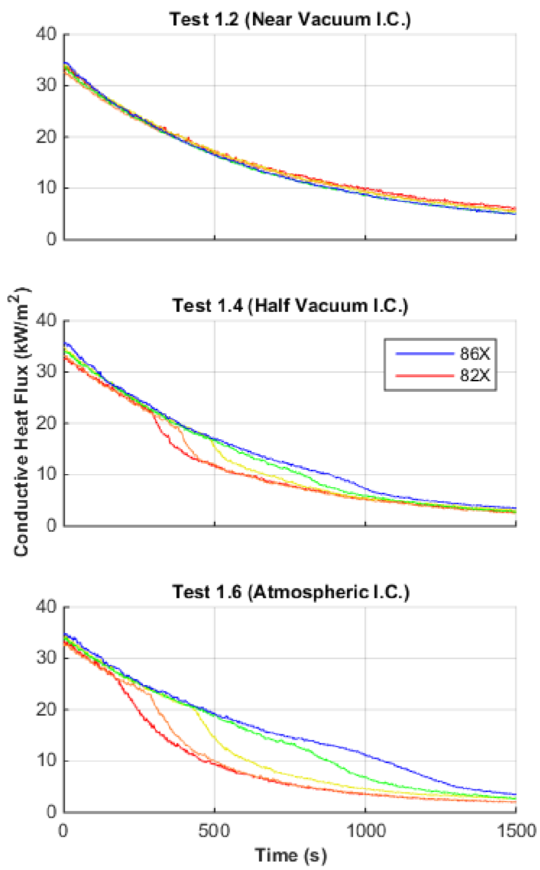

Figure 5-27: Conduction heat flux as measured on the HTP after terminating steam supply

There are several explanations for this segregation of the species.

- The molecular weight of air at 29g/mol is significantly greater than water at 18g/mol.
- The steam enters near the top of the vessel, hot and superheated.
- The condensation entrains the noncondensable gas towards and down the plate.
- The small diameter of the lower HPC constrains mixing.

The depth of analysis on the influence of noncondensable gases is limited to these observations as there is no reliable method of evaluating local gas concentrations. It is clear that the vapor and gas space may not be considered well mixed, and evidence suggests that the noncondensable concentrations in the upper region of the HPC do not significantly increase when the initial air pressures are greater.

5.7 Accounting for Low Measured Conduction Heat Flux

The measured conduction heat flux appears to under predict the true heat transfer through the plate. As show in Table 5-5, the conduction heat flux is measured roughly 40% lower than the heat balance suggests. There are several factors that may contribute to this problem:

5.7.1 Edge Effects

Heat transfer through the plate is not 1-D heat conduction as was assumed. Edge effects on the sides of the plate lead to temperature gradient variations along the width of the plate. The temperature gradient is lowest where the heat flux is measured (the plate centerline) and greatest on the very edges of the plate.

To investigate this effect, a set of thermocouples were installed to measure the temperature across the edge of the plate and a short distance along the cooling pool and containment vessel wall. These were installed at the elevation of the 83X thermocouples for the second set of tests.

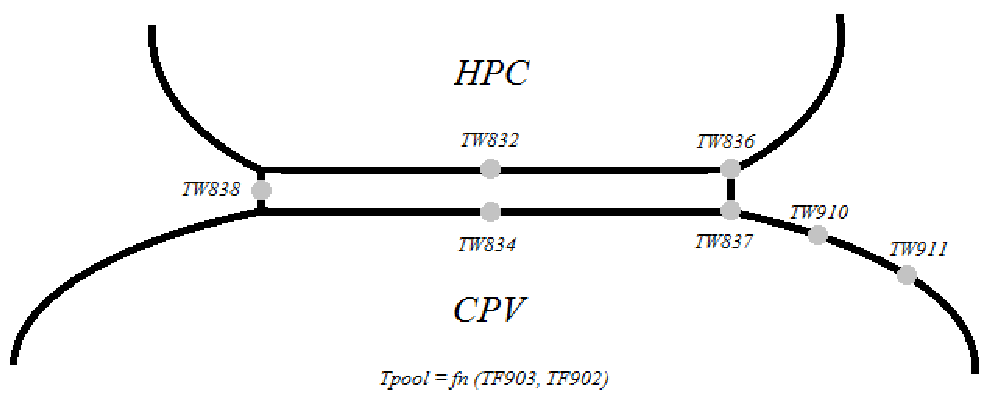

Figure 5-28: Thermocouple placement for investigating edge effect

A data point (t = 2000s) from the quasi-steady region of Test 2.1 is employed in the following evaluations. The measurements involved are presented in Table 5-6. The bulk temperature of the pool at this elevation is taken as the elevation weighted average of TF902 and TF903.

Table 5-6: Measurements involved in evaluating the edge effect

Parameter	**Value**
TW832	123.0 °C
TW833	100.3 °C
TW834	73.9 °C
TW836	145.7 °C
TW837	57.8 °C
TW838	110.0 °C
TW910	17.8 °C
TW911	16.8 °C
Tpool = (0.9 TF903 + 0.7 TF902) / 1.6	15.9 °C
Heat flux as required from energy balance	35.8 kW/m^2
1-D conduction heat flux measured	21.0 kW/m^2

5.7.1.1 Interpolation

During the course of the tests, measurement from TW836 and TW837 indicate a much greater temperature gradient at the edge of the plate than at the centerline. The temperature distribution along the width of the plate is known only at the edges and at the centerline; an arbitrary temperature profile may be assigned to estimate the average heat flux across the width of the plate.

Linear temperature profile – This temperature profile is the least credible but should provide an upper bound to the increase in heat transfer from edge effects. The average temperature gradient between the centerline and the edge can provide an average heat flux.

$$\overline{\dot{Q}''_{83X}} = k_{HTP} \cdot \frac{(TW832 - TW834) + (TW836 - TW837)}{2\, Th_{HTP}} \tag{4.86}$$

Quadratic temperature profile – This temperature profile is more credible than a linear fit as it implies the rate of change of plate temperature in the lateral direction is continuous and equal to zero at the centerline. This is a second order polynomial fit.

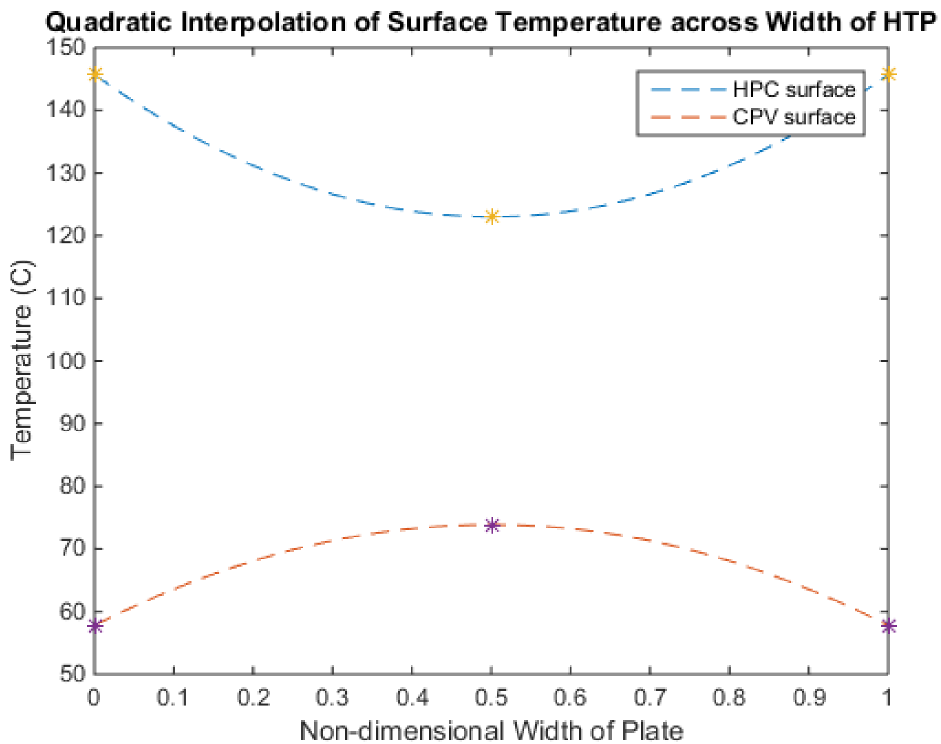

Figure 5-29: Quadratic temperature profile interpolated across width of the heat transfer plate

5.7.1.2 Fin Effect

As opposed to estimating the edge effects by interpolating for the surface temperatures across the width, the fin effect approach may be considered. The azimuthal heat flows through the vessel walls in contact with the plate likely account for the majority of the increased heat flux at the edge. This heat flow can be calculated if the vessel walls are considered as fin extensions from the heat transfer plate.

In this case, the length of the fin is assumed to be half of the circumference of the vessel. The vessel wall temperature equal to the bulk pool temperature at the end of the fin and is equal to TW837 at the base of the fin. Equation 4.87 can be used to evaluate the heat rate attributable to the fin effect.

$$\dot{Q}_{fin} = \sqrt{hPkA_c}(T_{base} - T_{bulk}) \tag{4.87}$$

Where

h = the natural convection heat transfer coefficient assumed to be 800 W/m^2-K

P = perimeter of fin taken as height of HTP = 5.64 meters

k = thermal conductivity of SS316 = 16.3 W/m-K

A_c = cross sectional (axial) area of vessel wall = 0.036 m^2

The result of this calculation is multiplied by a factor of 2 to account for both edges of the plate and then divided by the total plate area to define a contribution to the average heat flux.

5.7.1.3 Calculated Average Heat Flux for Edge Effect Considerations

Table 5-7: Average heat flux after accounting for the edge effects

Approach Taken	**Average Heat Flux**
Base Case	21.0 kW/m^2
Linear profile	29.3 kW/m^2
Quadratic profile	26.6 kW/m^2
Fin effect	25.3 kW/m^2

While accounting for the edge effect increases the average heat flux observed, neither method fully satisfies the energy balance. Edge effects may contribute to the overall discrepancy in the energy balance, but they do not explain why the local heat flux and heat transfer coefficients measured at the centerline of the plate are unusually low when compared to existing condensation models. The edge effects act to increase the heat transfer on the edges, not to decrease it at the centerline. If the plate was widened considerably, the influence of the edge effects would decrease and the average temperature gradient across the thickness of the plate would approach the centerline temperature gradient measured in these tests.

5.7.2 Spatial Error on Thermocouple Measurements

A source of error contributing to the low measured heat flux at the centerline of the plate may be the spatial error associated with the location of the thermocouple measurements. Slots were drilled in the heat transfer plate for placing the embedded thermocouples. These slots are rectangular with a depth and height of 0.083 inches. It is possible the temperature being measured by the thermocouple is attributable to some location within the slot, as opposed to the surface of the plate.

Table 5-8: Average heat flux accounting for spatial error

Assumed Measurement Location	**Average Heat Flux**
Base Case (surface)	21.0 kW/m^2
Center of slot	22.2 kW/m^2
Inside of slot	23.6 kW/m^2

5.7.3 Temperature Field Distortion

An additional source of error that may relate to the low measured conduction heat flux is distortion of the temperature field due to the slots, thermal paste, and thermocouples themselves. The magnitude of error or bias that can be associated to distortion of the temperature field is challenging to evaluate with any confidence due to the complexity of the geometry in question (Figure 5-30). In this case, the K type thermocouples and boron nitride thermal paste both have greater thermal conductivities than the SS316 HTP. This could contribute to a reduced heat flux measurement as the thermal resistance across the depth of the plate is reduced by introducing the embedded thermocouples [27]. The degree to which the temperature field is distorted by the presence of the thermocouples is unknown; it is unclear if this effect is sufficient to complete the energy balance.

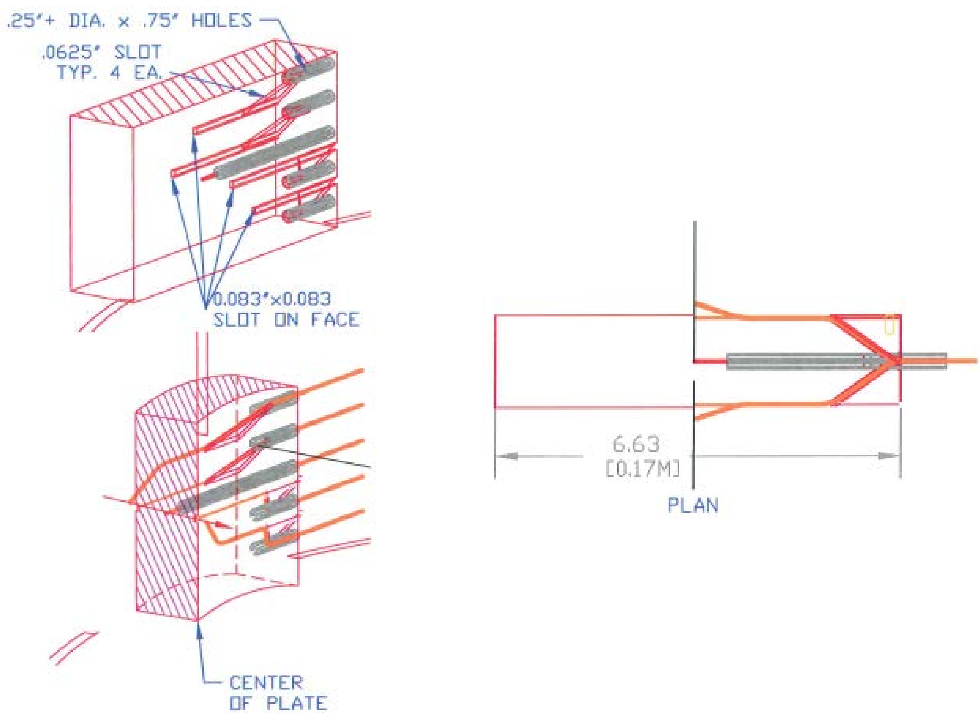

Figure 5-30: Diagram of embedded thermocouple placement

5.7.4 Challenges with Surface Temperature Measurement

Experimentally measuring surface temperatures has always been challenging. The discontinuity between the environmental temperature and the surface temperature offers difficulties not encountered in other types of temperature measurements. Often times, non-contact measurement methods such as the use of infrared sensors are ideal for measuring surface temperatures as these methods do not influence the temperature field. However, in many applications such as this one, embedded thermocouples are the most suitable way to measure surface temperatures and associated heat fluxes.

In an investigation similar to this one, Kim et al. [28] characterized condensation rates with use of embedded thermocouples measuring a temperature gradient across a tube wall. The authors state that this measurement method is generally not adopted due to large measurement uncertainties of the inner and outer surface temperatures. The authors report a need to calibrate this method in order to evaluate accurate surface measurements. This was done by applying a known heat flux to the tube and then applying a correction factor on the subsequent test results.

5.8 Correction for HTP Temperatures

Whichever the reason for the low measured heat flux, a correction method is proposed to evaluate an effective heat flux and heat transfer coefficient. This calculation assumes that there are no environmental heat losses (Assumption 1) and that all of the heat removal associated with the measured phase change occurs entirely on the unsubmerged surface area of the heat transfer plate. This allows for the evaluation of an average heat flux and a representative average temperature gradient on the plate. This temperature gradient is placed across the measured plate midline temperatures (TW8X3) to determine effective surface temperatures which can be used to evaluate a heat transfer coefficient.

Section 4.2.8 of this report describes the calculations involved. Figure 5-31 shows the corrected heat flux on the plate for each of the tests from the second set. These quasi steady tests were more suitable than the first set of test for the averaging that was required. The corrected heat flux is significantly higher for all of the tests evaluated.

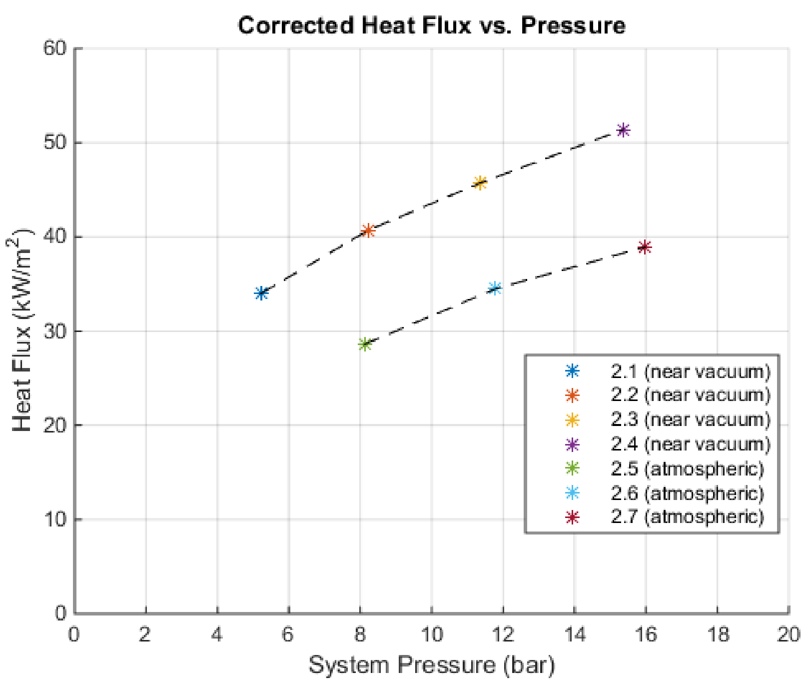

Figure 5-31: Condensation heat flux calculated from alternate method vs. system pressure

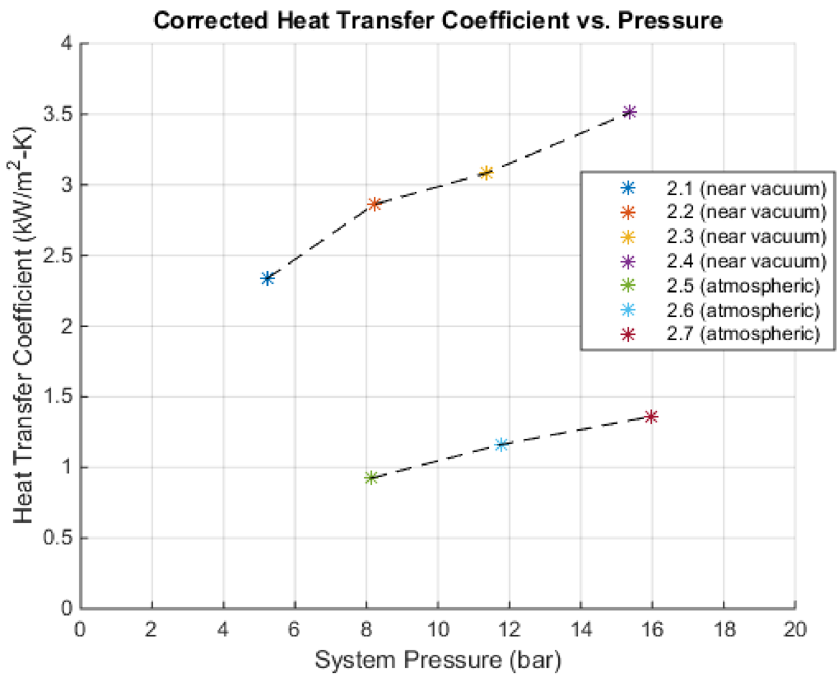

Figure 5-32: Heat transfer coefficients calculated from alternate method vs. system pressure

The difference between the noncondensable initial conditions is evident with this method. While the HTP thermocouples don't measure much of a difference in the heat flux on the upper half on the HTP, the condensate level rise reflects the reduced condensation rate on the lower portion.

The HTP thermocouple measurements (Figure 5-24 and Figure 5-25) suggested no influence on the heat transfer coefficient from changes in pressure. Conversely, this alternate method suggests that pressure may enhance heat transfer coefficients.

5.9 Uncertainty Quantification

To clarify displaying the results, the evaluated uncertainty of heat flux and heat transfer coefficient were omitted from the previous figures. Figure 5-33 and Figure 5-34 shows the heat flux, heat transfer coefficient, and associated uncertainties for an individual test. Figure 5-35 and Figure 5-36 shows the uncertainty evaluation of the corrected heat flux and heat transfer coefficients.

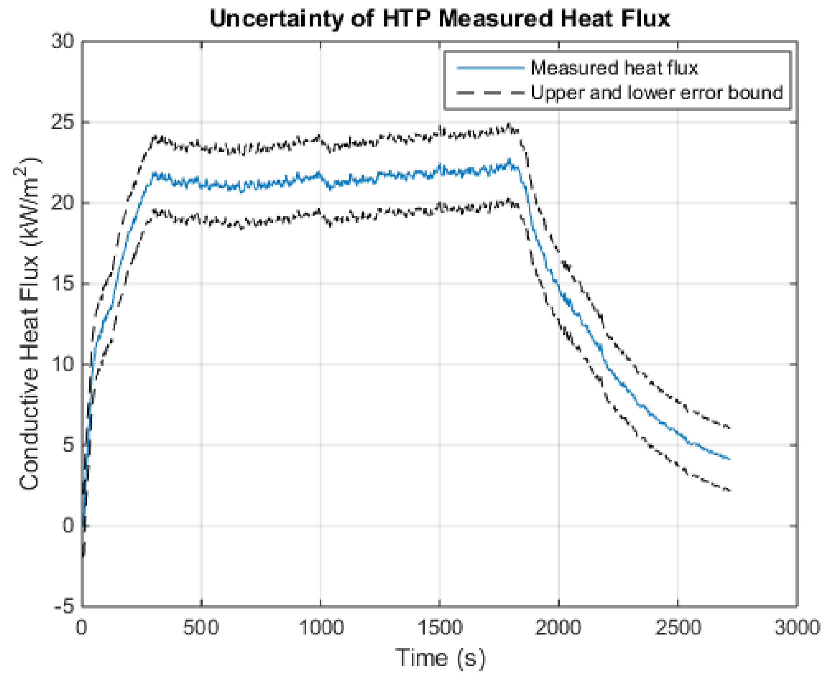

Figure 5-33: Uncertainty of heat flux as measured with HTP measurements (from Test 2.1)

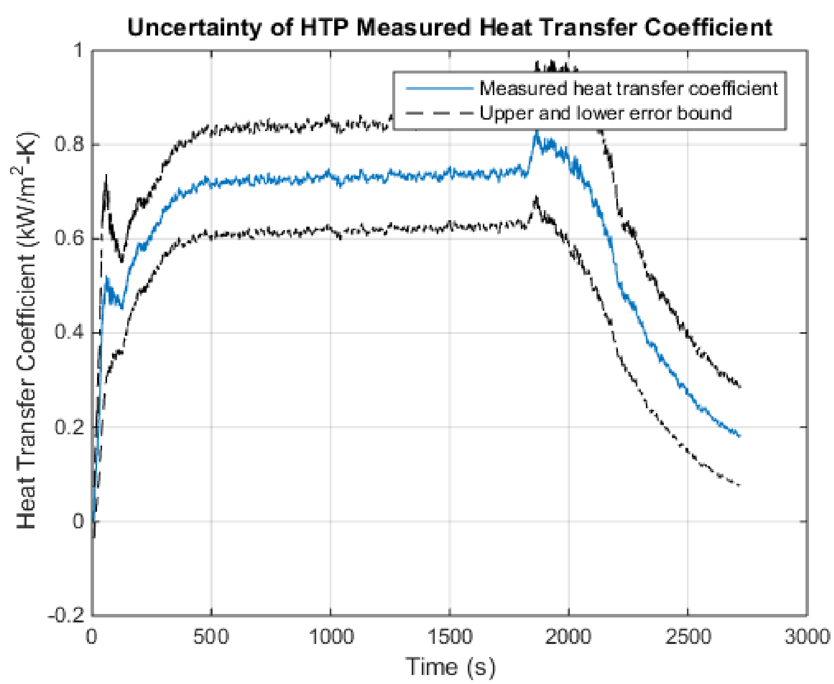

Figure 5-34: Uncertainty of heat transfer coefficient as measured with HTP measured (from Test 2.1)

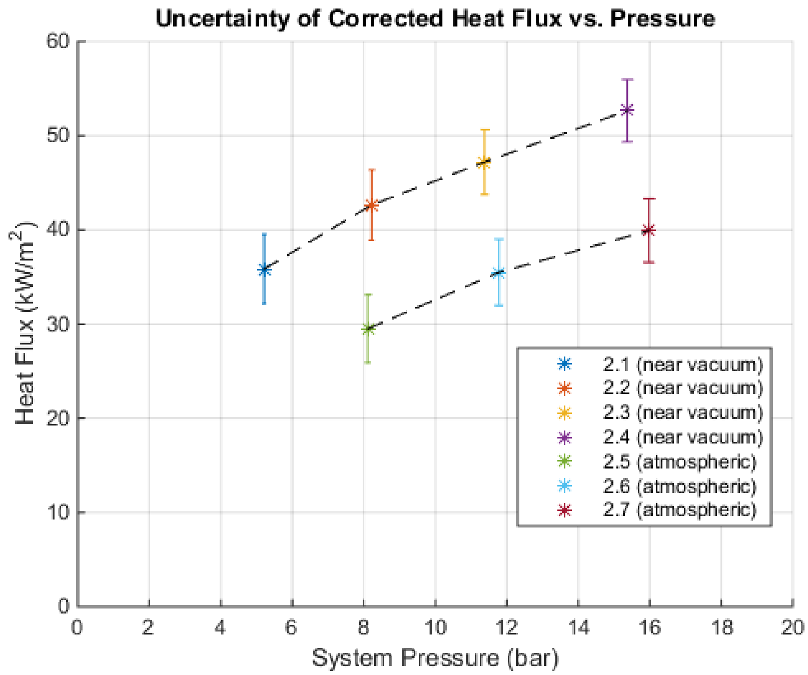

Figure 5-35: Uncertainty of heat flux as calculated with corrected surface temperatures

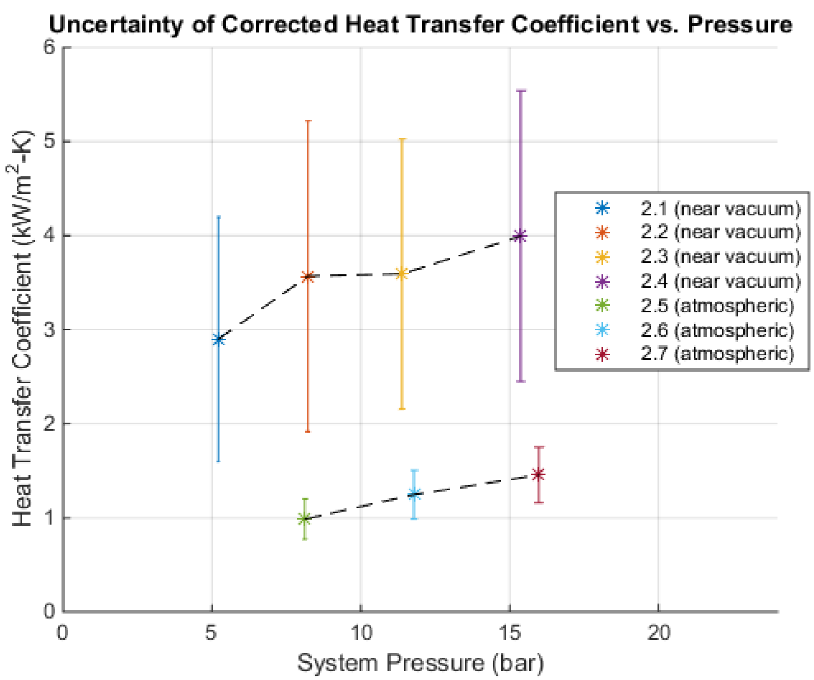

Figure 5-36: Uncertainty of heat transfer coefficient as calculated with corrected surface temperatures

The correction method for the heat transfer coefficient appears to be quite sensitive to instrument error and that confidence in the in the validity of the result may be limited.

6 Conclusions

6.1 Summary

A total of 13 condensation tests were conducted with the MASLWR test facility. Two unique testing approaches (transient vs. quasi steady) were employed, providing diversity in the data collected. Steam condensation in the containment was evaluated between pressures of approximately 4 and 21 bar with three different static inventories of noncondensable gas. Condensation and heat transfer rates were evaluated employing several methods, notably from measured temperature gradients in the HTP as well as measured condensate formation rates. A detailed mass and energy accounting was used to assess the various measurement methods and to support simplifying assumptions required for the analysis. Condensation heat fluxes and heat transfer coefficients are calculated and presented as a function of pressure to satisfy the objectives of this investigation.

6.2 Remarks

The heat transfer coefficients calculated using the measured HTP wall temperatures are considerably lower than popular condensation models would predict. The experimentally calculated value of between 700 and 800 W/m^{2}K is just a fraction of the Nusselt prediction, evaluated to be about 5000 W/m^2-K for the conditions of the test. The correction for surface temperatures proposed in Section 5.8 leads to effective heat transfer coefficients in the range of 3000 W/m^{2}K.

The Uchida and Tagami models are the most widely employed condensation models used in containment analysis. The correlations they developed are attractive in their simplicity, as they relate the heat transfer coefficient to a single parameter, the noncondensable weight fraction. Dehbi expanded upon their work by considering the influence of additional parameters such as pressure and condensing length. According to these experimental models, the air mass fraction required to achieve the same heat transfer coefficients as evaluated with the HTP surface temperatures in the MASLWR facility would have to be roughly 0.3 (Figure 6-1). During the tests, the total air mass fractions were generally much lower than this (between 0.01 and 0.4 at the extremes of testing conditions). The corrected heat transfer coefficients on the order of 3000 W/m^{2}K share considerably better agreement with these correlations. Regardless, application of these models to the MASLWR containment is not appropriate due to the very poor mixing of steam and gas.

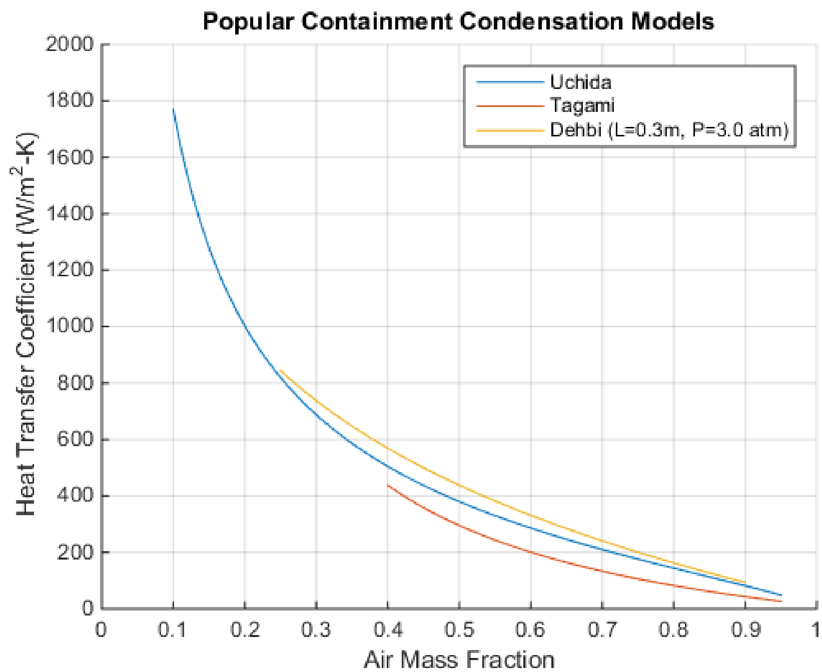

Figure 6-1: Condensation heat transfer coefficient predictions from popular models

A possible explanation for the low measured heat transfer coefficients is a localized concentration of noncondensable gas at the film interface. The theoretical work of Minkowycz and Sparrow concluded that even small concentrations of noncondensable gasses may reduce heat transfer coefficients to within the range observed in these tests. However, if non condensable gases were degrading the heat flux on the plate, one would expect a further reduction in the measured heat flux when the initial air inventory was increased. This was not observed with the tests. The noncondensable gases concentrate at the bottom of the containment while the vapor in the upper containment remains mostly pure.

The energy balance performed with the analysis indicates agreement between the heat removed from the HPC and heat supplied to the CPV and supports the assumption that the large majority of condensation is occurring on the heat transfer plate and not on the insulated surfaces of the HPC. The calculations employed for the change in CPV internal energy were admittedly somewhat contrived (recall extrapolating data points) introducing an unknown degree of uncertainty.

However, the result of the comparison suggests that environmental heat losses were low and the majority of heat removed from the HPC was conducted through the plate. The energy balance also indicates that the conductive heat transfer measured with the HTP thermocouples was systematically lower than the other two measurements.

An explanation that has been proposed for this inconsistency is that the heat flux across the plate varies significantly along its width and, at the midline, is being measured at the lowest value. The HPC and CPV vessels conduct heat azimuthally and across the edges of the plate where the structures are welded together. The heat flux is hypothesized to be much greater along the edges of the plate and the integration of the heat flux would perhaps match the heat removal calculated from the other methods. Figure 6-2 is a diagram of the scenario described, including representative temperature profiles along both sides of the plate. This concept has been referred to as the fin effect since the HPC and CPV vessels act as extensions of the heat transfer plate.

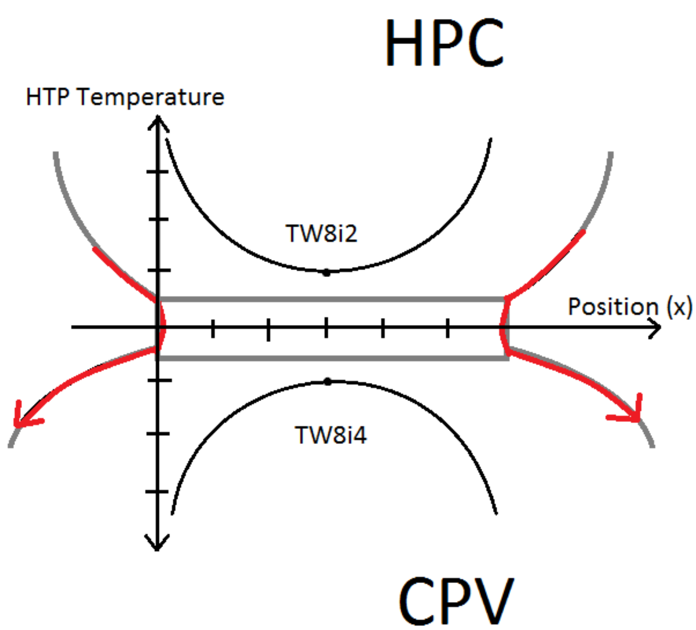

Figure 6-2: Diagram of the theorized fin effect

At a glance, the fin effect theory is attractive for explaining the unusually low heat transfer coefficients measured with the facility. A valid argument is made that heat transfer is not entirely a 1-D conduction problem as per Assumption 7. While this fin effect likely contributes to the incomplete energy balance, it fails to explain why the local heat transfer coefficients at the midline of the plate are so much lower than expected.

It seems likely that the heat transfer plate thermocouples are not accurately measuring the surface temperature on either side. The thermocouples have been fixed to the plate since the construction of the facility and cannot be individually removed and calibrated. It could be that distortion of the thermal field from the measurement device and difficulties in accurately measuring interface temperatures lead to this discrepancy. As was reported by Kim et al. [28], the best solution may be to calibrate the system by applying a known heat flux.

The objectives of this investigation included determining whether there was a pressure effect on condensation heat transfer rates. The results of the work remains somewhat indecisive on this matter. The heat transfer coefficient, as measured with the HTP thermocouples, suggest that there is no pressure effect on heat transfer rates. Many of the prior works relating to pure vapors support this conclusion, including implications of the Nusselt theory. However, most investigation into the pressure effect in the presence of noncondensable gases conclude that heat transfer coefficients are substantially improved with increasing pressure. This suggests that increased pressure may be reducing the heat transfer resistances involved with diffusion across the steam-vapor boundary layer (which doesn’t exist with pure vapors). Conversely to the HTP measurements, the alternate method for calculating heat transfer coefficients employed in the investigation seemed to indicate a pressure dependence however the uncertainties invoked with this method appear to be significant.

6.3 Future Work

The MASLWR facility that provided the opportunity for this investigation has been largely dismantled. Use of the renovated facility which includes a brand new HPC and CPV will likely not be offered for academic investigations as it embodies highly proprietary technology that will play a critical role in certification of the NuScale Power Module™ design.

To continue with the experimental investigation, the dismantling of the facility presents an intriguing opportunity. While this would require substantial funding, the old HPC and CPV, currently in storage, could be refurbished into a sort of separate effects facility. The proposed work would involve replacing the CPV with a thin rectangular flow channel along the heat transfer plate. Cooling on the pool side of the plate could be performed with a single phase flow, allowing for a very accurate average heat flux evaluation. Additionally, a pressurized vessel may be connected to the drain at the bottom of the containment. This would allow condensate to continuously drain into the storage tank during testing and may help flush out any noncondensable gas. The steam would continue to be supplied by the secondary system of the (now renovated) MASWLR facility. This separate effects facility would be capable of achieving steady state conditions and could address many of the limitations encountered with this investigation.

7 Bibliography

[1] J. N. Reyes, J. Groome, B. G. Woods, K. Abel, Y. Yao and Y. J. Yoo, "Testing of the multi-application small light water reactor (maslwr) passive safety systems," *Nuclear Engineering and Design, 237,* no. 18, pp. 1999-2005, 2007.

[2] J. G. Collier, Convective Boiling and Condensation, 3rd ed., New York City: Oxford University Press Inc., 1980.

[3] Wolverine Tube, Inc., "Chapter 7: condensation on external surfaces," in *Engineering Data Book III*, 2007.

[4] A. Faghri, Y. Zhang and J. Howell, "Advanced Heat and Mass Transfer (e-Book)," 2010. [Online]. Available: https://www.thermalfluidscentral.org/e-books/book-intro.php?b=37. [Accessed 22 April 2015].

[5] W. Nusselt, "The surface condensation of water vapor," *Zeitschrift Ver. Deut. Ing.,* vol. 60, pp. 541-546, 1916.

[6] W. Stender, *Z. Ver. deut. Ing.,* vol. 69, p. 905, 1925.

[7] L. Bromley, "Effect of heat capacity of condensate," *Industrial and Engineering Chemistry,* vol. 44, p. 2966, 1952.

[8] E. Sparrow and J. Gregg, "A boundary layer treatment of laminar film condensation," *J. Heat Transfer,* vol. 21, no. Series C, pp. 13-18, 1959.

[9] G. Poots and R. Miles, "Effects of variable physical properties on laminar film condensation of saturated steam on a vertical flat plate," *Int. J. Heat Mass Transfer,* vol. 10, pp. 1677-1692, 1967.

[10] M. Chen, "An analytical study of laminar film condensation Part 1-Flat Plates," *J. Heat Transfer,* vol. 83, no. Series C, pp. 48-55, 1961.

[11] H. Brauer, "Stromung und warmeubergang bei reiselfilmen," *VDI Forschung,* vol. 22, pp. 1-40, 1956.

[12] D. Butterworth, "Film condensation of pure vapor (chapter 2.6.2)," in *Heat Exchanger Handbook,* Washington, DC, Hemisphere, 1983.

[13] M. Corradini, "Fundamentals of Multiphase Flow," 1997. [Online]. Available: http://wins.engr.wisc.edu/teaching/mpfBook/. [Accessed 22 April 2015].

[14] S. Sukhatme and W. M. Rohsenow, "Heat transfer during film condensation of liquid metal vapor," Dept of Mech Eng, MIT, 1964.

[15] S. Khandekar and M. Krishnamurthy, Dropwise Condensation on Inclined Textured Surfaces, New York City: Springer Science+Buisiness Media, 2014.

[16] N. Maheshwari, P. Vijayan and D. Saha, "Effects of non-condensable gases on condensation heat transfer," Bhabha Atomic Research Centre, Mumbai.

[17] W. Minkowycz and E. M. Sparrow, "Condensation heat transfer in the presence of noncondondensables, interfacial resistance, superheating, variable properties, and diffusion," *International Journal of Heat and Mass Transfer,* vol. 9, no. 10, pp. 1125-1144, 1966.

[18] H. Uchida, "Evaluation of post accident cooling systems of LWR's," in *Int. Conf. Peaceful Uses of Atomic Energy, 13, 93*, 1965.

[19] T. Tagami, "Interim report on safety assesments and facilities establishment," No 1 Japanese Atomic Energy Research Agency, 1965.

[20] A. A. Dehbi, "The effects of noncondensable gases on steam condensation under turbulent natural convection conditions," PhD Thesis, Massachusetts Institute of Technology, 1991.

[21] J.-W. Kim, Y.-G. Lee, H.-K. Ahn and G.-C. Park, "Condensation heat transfer characteristic in the presence of noncondensable gas on natural convection at high pressure," *Nuclear Engineering and Design 239,* pp. 688-698, 2009.

[22] J. Casey, "High pressure condensation heat transfer in the evacuated containment of a small modular reactor," M.S. Thesis, Oregon State University, 2013.

[23] B. Bristol, "Free convective heat transfer at the OSU MASLWR test facility," M.S. Thesis, Oregon State University, 2015.

[24] J. N. Reyes and J. B. King, "MASLWR integral system test facility scaling analysis," Oregon State University, 2003.

[25] S. Modro, "Multi-application small light water reactor final report," Technical report, Idaho National Engineering and Envrionmental Laboratory, 2003.

[26] OSU MASLWR Records, "Test facility description report (OSU-MASLWR-07001-R2)," Oregon State University, 2011.

[27] M. Attia and L. Kops, "Distortion in Thermal Field Around Inserted Thermocouples in Experimental Interfacial Studies—Part II: Effect of the Heat Flow Through the Thermocouple," *J. Eng. Ind,* vol. 110, no. 1, pp. 7-14, 1988.

[28] J. S. Kim and H. C. No, "Turbulent film condensation of high pressure steam in a vertical tube," *Int. J. Heat Mass Transfer,* vol. 43, pp. 4031-4042, 2000.

[29] L. E. Herranz, M. H. Anderson and M. L. Corradini, "A diffusion layer model for steam condensation within the AP600 containment," *Nuclear Engineering and Design 183,* pp. 133-150, 1998.

[30] OSU MASLWR Records, "Test facility volume and elevation report (OSU-MASLWR-10003-R1)," Oregon State University.

[31] D. J. Wilhelm, "Condensation of metal vapors: mercury and the kinetic theory of condensation," UNT Digital Library. http://digital.library.unt.edu/ark:/67531/metadc67199/, Argonne.

[32] A. Colburn and O. Hougen, "Design of cooler condensers for mixtures of vapors with noncondensing gases," *Ind. Eng. Chem,* vol. 11, no. 26, pp. 1178-1182, 1934.